Phase-Contrast X-Ray Computed Tomography

（位相型X線コンピュータトモグラフィ）

百生敦

①

Phase-Contrast X-Ray Computed Tomography

(位相型X線コンピュータトモグラフィ)

ATSUSHI MOMOSE

1996

This work was published in

A.Momose,

"Demonstration of phase-contrast X-ray computed tomography using an X-ray interferometer."

Nucl. Instrum. Meth., A**352**, 622-628 (1995).

A.Momose, T. Takeda, and Y. Itai,

"Phase-contrast X-ray computed tomography for observing biological specimens and organic materials."

Rev. Sci. Instrum., **66**, 1434-1436 (1995).

A.Momose and J. Fukuda,

"Phase-contrast radiographs of nonstained rat cerebellar specimen."

Med. Phys., **22**, 375-380 (1995).

A.Momose, T. Takeda, and Y. Itai,

"Contrast effect of blood on phase-contrast X-ray imaging."

Acad. Radiol., **2**, 883-887 (1995).

A.Momose, T. Takeda, Y. Itai, and K. Hirano,

"Tomographic image reconstruction using X-ray phase information."

SPIE Proc. Vol. 2708, 674-684 (1996).

A.Momose, T. Takeda, Y. Itai, and K. Hirano,

"Phase-contrast X-ray computed tomography for observing biological soft tissues."

Nature Medicine, **2**, 473-475 (1996).

T. Takeda, A.Momose, Y. Itai, J. Wu, and K. Hirano,

"Phase-contrast imaging using syschrotron X-rays for detecting cancer lesions."

Acad. Radiol., **2**, 799-803 (1995).

Contents

1 General Introduction **3**

1.1 Introduction 3

1.2 X-Ray Interferometer 8

1.3 X-Ray CT 11

2 Phase-Contrast X-Ray Imaging **15**

2.1 Introduction 15

2.2 Imaging Using an X-Ray Interferometer 16

2.3 Phase Determination from Interference Patterns 21

2.4 Quantitative Analysis of X-Ray Phase Shift 31

3 Tomographic Image Reconstruction **34**

3.1 Introduction 34

3.2 Principle of Image Reconstruction 35

3.3 Quantity Revealed by Phase-Contrast X-Ray CT 38

3.4 Sample Rotation in Phase-Contrast X-Ray CT 42

4 Phase-Contrast X-ray Tomograms **50**

4.1 Introduction 50

4.2 Preliminary Studies Using Test Object 51

4.3 Application to Biological System 63

4.4 Interpretation of Image Contrast 66

4.5 Future of Phase-Contrast X-Ray Imaging 75

5 Concluding Remarks **78**

Acknowledgments **81**

References **82**

Chapter 1

General Introduction

1.1 Introduction

Various types of imaging techniques using X-rays have been developed for many kinds of applications. Transmission imaging of hard X-rays is one of the most serviceable because it can depict the inside structure of an object nondestructively. In medicine, especially, studies for practical uses of this technique were started early in its history. In recent years, X-ray transmission imaging has been developed into three-dimensional imaging—X-ray computed tomography (CT) [1]. Furthermore, the recent development of synchrotron radiation (SR) sources has made possible sophisticated imaging techniques that use the attractive properties of SR, such as high intensity, energy selectivity, and high degree of collimation. For example, X-ray CT of a high spatial resolution has been developed to contribute to materials science [2–7]. Moreover, SR is expected to increase the image quality of medical images [8].

But application of the X-ray transmission imaging is limited mainly to the observation of objects that are semitransparent to X-rays. The image contrast in X-ray transmission images is produced by X-ray absorption (including scattering loss) along the X-ray beam path inside an object. Materials of high X-ray absorbance distributed within an object cause X-ray shadows. In general, elements having higher atomic numbers produce darker X-ray shadows. Consequently, the

fine structures can be revealed easily in an object that contains heavy elements. Conversely, the observation of organic materials consisting of light elements is not successful using the X-ray transmission imaging. This is because the amount of X-rays absorbed by the light elements is not large enough to be detected. Hence, sufficient image sensitivity cannot be expected with organic materials or biological soft tissues consisting mainly of hydrogen, carbon, nitrogen, and oxygen. Such objects are too transparent to hard X-rays. Therefore, when possible, the image contrast is enhanced with a contrast medium. Studies for medical diagnosis using SR also assume the use of such stains as iodine for contrast enhancement. This is a common problem in X-ray CT.

In contrast, phase-contrast X-ray imaging [9–11], which produces image contrast that depends on the distribution of the X-ray phase shift, is known to be sensitive to light elements. This is because the X-ray phase shift is substantial enough to be detected even when absorption is almost zero. In the hard X-ray energy region, the cross section of the X-ray phase shift is about a thousand times greater than that of the X-ray absorption. The weakly absorbing objects therefore can be observed with X-ray phase-contrast without the need for contrast enhancement. Moreover, this high sensitivity contributes to reducing the X-ray dose. The X-ray dose is a crucial consideration in the observation of biological objects that must not sustain excessive radiation damage. Thus, phase-contrast imaging is attractive for internal observation of weakly absorbing objects.

Phase-contrast imaging creates image contrast through the shift in the phase of X-rays that is caused by an object. The X-ray phase information, however, is not obtained only by measuring the intensity of X-rays. To obtain the phase information, it is necessary to create a reference X-ray beam and then to superpose it on the X-ray beam transmitted through an object (object beam). If these two beams are coherent, an X-ray interference pattern can be seen that corresponds to the distribution of the phase shift caused by the object.

Such coherent beams are created by use of an X-ray interferometer. But developing an interferometer for the X-ray region is not as easy as making one for the visible light region. The X-ray wavelength is extremely short; consequently, the optical paths must be stable, with deviations within subangstrom tolerances. Thirty years ago, Bonse and Hart [12] created a stable X-ray interferometer by cutting the entire body of the interferometer monolithically from a block of perfect silicon crystal. All optical elements were aligned accurately at the lattice level, and the optical paths no longer drift so much. Thus, Bonse and Hart opened up the possibility of X-ray interferometry. One attractive application of the X-ray interferometer is phase-contrast imaging, and some demonstrations of the phase-contrast imaging have been reported [9–11]. The research described in this thesis also utilized this X-ray interferometer.

Bonse and Hart reported the first phase-contrast X-ray image, using a plano-concave epoxy lens as a test object [9]. Interference fringes of equal thickness were visible. Later, Ando and Hosoya applied this technique to biological specimens, such as human bone [10]. The image sufficiently demonstrated the higher sensitivity of phase-contrast X-ray imaging compared to that of absorption-contrast X-ray imaging.

One demerit of phase-contrast imaging using the X-ray interferometer was the long exposure time required. This was because the energy band width of the coherent beams was narrow and the photon flux tended to be insufficient. Those images were obtained with characteristic X-rays from conventional X-ray generators. Consequently, obtaining an interference pattern took a few hours. The use of a SR source considerably shortened exposure time. Ref. [11] reported phase-contrast imaging of a human tooth with SR. Because the X-ray intensity was sufficient, it seems that the image quality increased, with exposure time of several tens of seconds.

Although the problem of the photon flux was solved by using a SR source,

study of phase-contrast imaging has not progressed as to its application, despite the attractive image sensitivity. Two other problems can be identified in the phase-contrast X-ray imaging reported to date. One is that a sample had to be sliced to a uniform thickness. In the earlier studies, a phase-contrast X-ray image was equivalent to an X-ray interference pattern. Therefore, unless the sample was of uniform thickness, interference fringes of equal thickness would superpose on the fringes caused by the inside structure of the sample. It is difficult to extract only the desired information about internal structures from such an interference pattern.

Another problem is that approaches were not made for quantitative analysis of interference patterns. Even if the sample is a slice of a uniform thickness, a process is needed for obtaining structural information from interference patterns. In the case of phase-contrast imaging, the distribution of the refractive index inside an object is related to the image contrast; the phase shift Φ corresponds to the projection of the distribution. Therefore, the ideal way to perform quantitative analysis of phase-contrast images is to evaluate the phase shift Φ. But it is difficult to determine Φ directly from an interference pattern. In general, the interference pattern I is written as

$$I = a + b\cos\Phi, \tag{1.1}$$

where a and b are the average fringe intensity and the fringe contrast. The Φ cannot be determined definitively because $2\pi n$ (n: integer) of phase uncertainty remains. Moreover, interference patterns vary depending on other optical conditions besides the phase shift caused by the object. For example, when the fabrication of the interferometer is incomplete, the phase difference between the two beams in the interferometer is no longer zero. Therefore, $\cos\Phi$ in eq. (1.1) should be replaced with $\cos(\Phi + \Delta)$, where Δ is the phase difference between the

object beam and the reference beam. The Δ is usually unknown, and this also prevents us from determining Φ. Moreover, the total thickness of the slice also influences the interference pattern. For example, if the slice happens to be a little thicker or thinner, the image contrast will be different, and occasionally inverse. The same object does not always create the same contrast. Furthermore, structural information is missing at the dark fringe area where the phase difference happens to be $2\pi(n+\frac{1}{2})$, due to an insufficiency of photons coming into this area.

These problems seem to have hindered the development of phase-contrast imaging. This thesis proposes and describes a technique for determining the distribution of Φ, or a phase-mapping image, from X-ray interference patterns. It is much easier to diagnose the internal structure quantitatively, by analyzing the phase-mapping image. Moreover, the technique for determining Φ allows us three-dimensional phase-contrast observation under tomographic configuration—i.e., phase-contrast X-ray CT. Our observation is no longer restricted to sliced samples. We have applied this novel technique to three-dimensional observations of biological soft tissues that are almost transparent to hard X-rays.

This thesis will describe the principle of phase-contrast X-ray CT. Also, the author will present results of the observations of nonstained biological soft tissues, obtained with synchrotron X-rays. In Chapter 2, methods for obtaining phase-mapping images will be described. Chapter 3 will show the principle of phase-contrast X-ray CT which reconstructs a three-dimensional image from phase-mapping images. Observation results and discussions will be presented in Chapter 4.

Phase-contrast X-ray CT involves the techniques of the X-ray interferometer and X-ray CT. The rest of this chapter describes their backgrounds briefly.

1.2 X-Ray Interferometer

Constructing an interferometer for the hard X-ray energy region is difficult because the entire system must be stable within a deviation distance shorter than the X-ray wavelength. As mentioned, Bonse and Hart overcame this difficulty about thirty years ago, with the idea of monolithic fabrication of the entire body of the interferometer from a perfect crystal. The historical aspect of phase-contrast X-ray imaging using the X-ray interferometer was briefly reviewed above; details of the X-ray interferometer is described here. The typical structure of the X-ray interferometer is shown in Fig. 1-1. Three parallel crystal slabs (S: beam splitter, M: mirror, and A: analyzer) are monolithically cut out from a crystal block having the same gaps. A photograph of one of the actually fabricated X-ray interferometers is shown in Fig. 1-2. Each slab functions as an X-ray half-mirror on satisfaction of the Bragg diffraction condition for the lattice plane perpendicular to the surface of the slab. Because all slabs are monolithical, the diffraction occurs at all slabs at the same time. Consequently, two coherent beam paths are created, as shown in Fig. 1-1. An interference pattern can be observed behind the analyzer (A).

The crystal slabs have the functions of beam collimation and monochromatization, and restrict the angular divergence and the energy band width of the X-ray beams in the interferometer. They help to cause interference even when the interferometer itself is incomplete due to deformation and/or fabrication error of the interferometer, or insufficient crystallinity of the silicon ingot. The interferometer obtains a higher degree of collimation and monochromatization when it is designed to use slabs of greater thickness. Also, thicker slabs better tolerate fabrication error in the interferometer. However, they also cause a decrease in beam intensity. Therefore, a slab thickness of about 1 mm is usually chosen; this is a practical value for performance of the interferometer and for convenience in

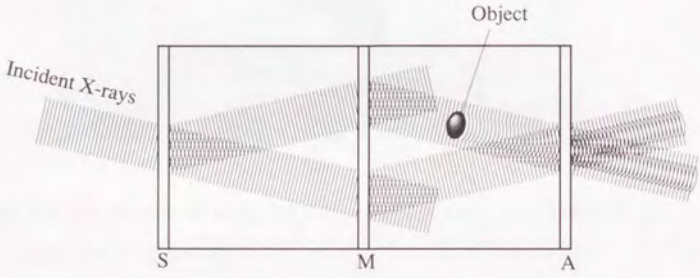

Fig. 1-1 An X-ray interferometer monolithically cut out from a crystal block. Three X-ray half-mirrors—the beam splitter (S), the mirror (M), and the analyzer (A)—are located in parallel and have equal gaps between them. Satisfying the diffraction condition, the beam incident to the interferometer is separated into two beams by the half-mirrors, thus creating two coherent beam paths. An object placed in one of the beam paths causes X-ray phase shift and a corresponding interference pattern can be seen.

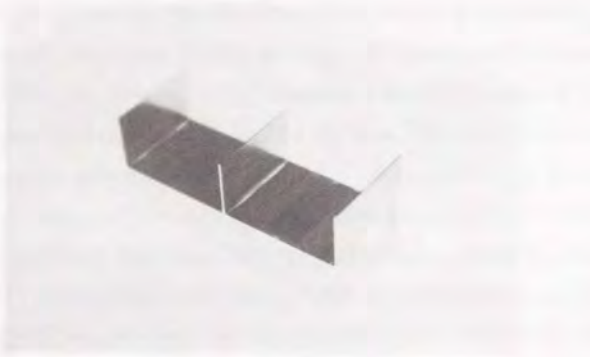

Fig. 1-2 Photograph of a typical X-ray interferometer monolithically cut out from a silicon crystal.

the fabrication.

Following are some considerations on coherence. The beam splitting by the slabs is based on dividing the amplitude. Therefore, when the interferometer is completely fabricated and no phase object is located in the beam paths, photons divided by the beam splitter (S) always meet in front of the analyzer (A) and interfere in phase. At every point within the beam cross section, interference occurs independently in the same manner. In this case, therefore, temporal and spatial coherence is not necessary to cause interference with this interferometer. When a phase object is placed in the beam path, however, some extent of coherency is required. The X-ray phase shift caused by the object makes a difference in the optical path lengths between the object beam and the reference beam. But the temporal coherence length (several microns), which is determined by the degree of monochromatization, is actually much greater than the difference in optical

paths. Therefore, the phase shift does not smear out the interference fringes.

As to the spatial coherence, the beam deflection due to the refraction must be considered. By passing through an object, the wavefront of X-rays bend as shown in Fig. 1-1. Because X-rays propagate in the direction perpendicular to the wavefront, X-ray photons divided by the beam splitter (S) then no longer impinge on the surface of the analyzer (A) at the same point. In the hard X-ray energy region, the amount of wavefront bending is small; the resultant beam deflection angle, but depends on the shape of the object, is typically 1 μrad. The shift of the entrance point to the analyzer due to the deflection is calculated as 50 nm in this case, assuming that the distance from the object to the analyzer (A) is 5 cm. The actual spatial coherence length is much greater than this value even for the conventional X-ray sources, and is enough to cause interference.

However, it should be noted that the performance of the slab as an X-ray half-mirror is affected by the beam deflection. The beam deflection angle is magnified in the crystal, and then finite spatial coherency influences the image quality. This is actually crucial to phase-contrast X-ray imaging with the X-ray interferometer. The details of this problem, and its solution, will be described in Chapter 3.

Moreover, spatial coherence is required when the gaps between the three slabs are not equal because the X-ray photons separated by the beam splitter (S) no longer meet at the analyzer (A). Therefore, tolerance of fabrication error depends on the spatial coherency of the X-ray beam incident to the interferometer. Assuming that the spatial coherence length is several microns, the error limit of the gaps is several tens of microns.

1.3 X-Ray CT

The discovery of X-rays was sensational because it enabled investigation of the inside structure of opaque objects as X-ray shadows. This property of X-rays was

especially attractive for medical diagnosis. Vigorous study of X-ray imaging was soon started, and has made practical contributions to medicine. However, three-dimensional structures inside an object were superposed onto two-dimensional X-ray films. The information obtained from the radiographic images, therefore, did not satisfy radiologists. They demanded, as a matter of course, new techniques that could resolve structures along the direction of X-ray propagation. Several techniques were tried for producing an image on an imaginary sectional plane of an object [13]. To form an image on a plane of interest located inside an object, the X-ray source and the film were moved synchronously, and other components were defocused. But the influence of the defocused component on the image was not negligible. It was found that more complete images could be constructed from the transmission images obtained in different directions of projection. This concept was reported in 1917 by Radon [14], who proved mathematically that the three-dimensional structure of an object can be determined from images projected from infinite directions. But enormous calculations were required to reconstruct an image. As a result, it was more than fifty years later that Hounsfield constructed an apparatus based on the principle—a prototypical CT scanner [1]—employing a computer. Nowadays, X-ray CT is used in materials science and industry in addition to medicine for three-dimensional investigation.

The geometrical relation of an object with the X-ray beam and the reconstructed image plane is illustrated in Fig. 1-3. X-ray transmission images are measured in different directions of projection. Usually, the direction of projection is varied by rotating an X-ray source and an X-ray detector synchronously around the object. Equivalent scan is achieved by rotating the object around the axis perpendicular to the X-ray beam path. In the case of Fig. 1-3, when the intensity of X-rays on the line perpendicular to the rotation axis are measured, X-ray CT produces an image (tomogram) on the imaginary sectional plane involving the line and perpendicular to the rotation axis. Images on other sectional

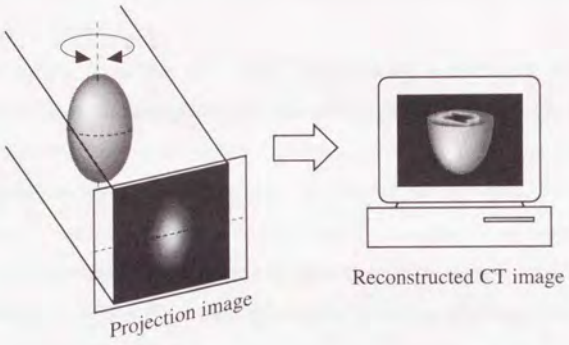

Fig. 1-3 Geometrical relation of an object with the X-ray beam and the reconstructed image in X-ray CT. Computed tomography reconstructs sectional images (tomograms) on the planes parallel to the X-ray beam path from projection images.

planes can be obtained by changing the probe line. Recently, X-ray digital image sensors have become available, and a series of tomograms are obtained using one scan. By stacking those tomograms, three-dimensional internal structures can be revealed nondestructively.

Recent developments in SR sources have contributed to increased performance in X-ray CT. Owing to the low divergence of SR beams, X-ray CT at a high spatial resolution (several microns) has been developed [3]. Moreover, because the X-ray energy is tunable, element-specific observations have been demonstrated, using absorption edge image subtraction [15]. In the hard X-ray energy region, heavy elements have their absorption edge, which corresponds to the onset of the excitation of electrons from a given core level to the continuum above the ionization limit. Therefore, transmission images obtained above and below the

edge differ, and the subtraction image between them shows the distribution of the specific element.

One problem remaining in X-ray CT is insufficient sensitivity in imaging objects consisting of light elements that do not absorb X-rays well. The technique of absorption edge image subtraction cannot be applied to light elements because their absorption edges do not exist in the hard X-ray energy region. Such objects, therefore, are usually stained with heavy elements to enhance image contrast. But using contrast media does not always bring success; in the case of medical diagnosis, moreover, injection of contrast media into the bodies of patients occasionally threaten their health. The objective of our study, therefore, is to make possible three-dimensional observation of the weakly absorbing objects without the use of contrast media. As mentioned, the technique of phase-contrast X-ray imaging meets this demand. The author therefore modified the X-ray interferometry and utilized the technique of X-ray CT for three-dimensional image reconstruction using X-ray phase information.

Chapter 2

Phase-Contrast X-Ray Imaging

2.1 Introduction

In order to make clear the physical sense of "phase-contrast" in this thesis, three levels of phase-contrast images obtained using the interferometer are explained. The first level is an X-ray interference pattern, obtained directly by recording the diffraction beam from the interferometer. Phase-contrast images reported before our study meant the interference patterns. As mentioned, interference patterns do not allow us to understand the internal structure of the object satisfactorily. The second level is an X-ray phase-mapping image that is obtained by processing X-ray interference patterns using an X-ray interferometry newly modified by the author. The phase-mapping image equivalently shows the projection of the refractive index, making more advanced analysis possible. The third level is phase-contrast tomograms, which are reconstructed by processing the phase-mapping images under a tomographic configuration.

In this chapter, preliminary observation results of interference patterns of rat cerebellar sections are first presented. With the observation, it is shown that X-ray phase-contrast imaging can reveal structures of nonstained biological soft tissues. Next, methods for obtaining phase-mapping images are described. Phase-contrast X-ray CT will be explained separately in the next chapter.

2.2 Imaging Using an X-Ray Interferometer

Although the observation results of thin slices of a human bone and a tooth have been reported [10,11], there was no experimental demonstration showing that X-ray phase-contrast imaging was sensitive to biological soft tissues. As a preliminary study, therefore, slices of a rat cerebellum were observed with the conventional phase-contrast X-ray imaging method to ascertain that image sensitivity was sufficient for soft tissues.

Figure 2-1 shows a schematic view of an experimental setup. The optics is almost the same as that in the earlier studies. We used SR from a bending section of a storage ring of the Photon Factory at Japan's National Laboratory for High Energy Physics. Experiments were performed at the station BL-8C_2. We selected 1-Å X-ray beam through a Si(220) double-crystal monochromator. Although the X-ray interferometer has a function of monochromatizing as mentioned, the monochromator was installed to prevent a white SR beam from impinging directly on the interferometer and causing the deformation of the interferometer due to heat load. The interferometer also used Si(220) reflection, and was aligned in a $(+,-)$ geometry against the monochromator. The interferometer was put on a goniometer of a vertical rotation axis because it was easy to align the interferometer. Instead, the intensity loss by the polarization factor $\cos 2\theta_B$ had to be accepted, where θ_B is the Bragg diffraction angle, because the SR beam at the station BL-8C_2 was linearly polarized in the horizontal plane.

Influence of higher harmonics contamination on interference patterns was negligible, as explained below. The diffraction angles of the Bragg-case monochromator and the Laue-case interferometer are slightly different because the refraction in the Si crystals affects the Bragg-case diffraction only [16]. The harmonics in the monochromatized beam, therefore, do not satisfy the diffraction condition of the interferometer at the same incident angle as that for the primary wavelength

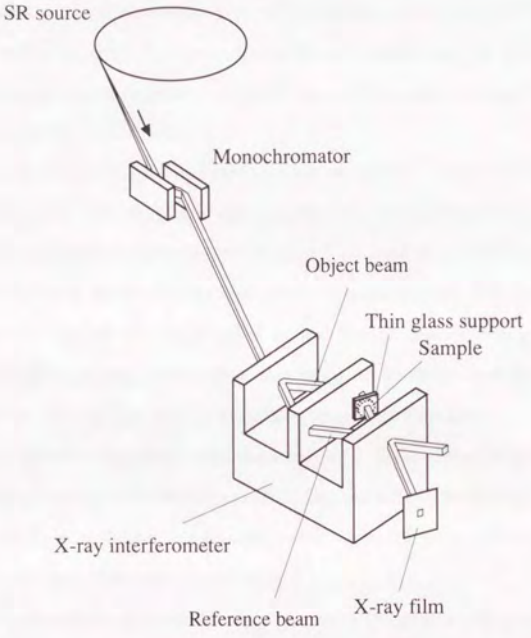

Fig. 2-1 Experimental setup to observe interference patterns using an X-ray interferometer. Synchrotron X-rays through a double-crystal monochromator impinged on the X-ray interferometer. A sliced sample supported by thin glass plates was placed in the object beam path. An interference pattern was detected with X-ray film.

beam. Thus, the harmonics were eliminated by precisely tuning the incident angle to the interferometer. For example, the intensities of 1-Å X-rays and the second harmonic (0.5-Å X-rays) in the outgoing beam from the interferometer were measured versus the rotation angle of the interferometer (Fig. 2-2). Diffraction peaks of 1-Å and 0.5-Å X-rays appeared in different angular positions. By selecting an appropriate angular setting, the second harmonic was prevented from passing through the interferometer.

The sample was prepared by cutting a rat cerebellum fixed in formalin into 1-mm thick slices. The formalin was prepared by dissolving formaldehyde in physiological salt solution at a concentration of 3.7%, and therefore do not contain heavy elements that absorb X-rays and create X-ray shadows. The sliced sample was placed into one of the beam paths of the interferometer, being supported between thin glass plates. The sample was wet with formalin and therefore was attached to the glass plates with the surface tension of formalin.

X-ray interference patterns were detected with X-ray films (Fuji X-ray film #50) placed about 15 cm downstream from the samples. The beam intensity of 1-Å X-rays in front of the sample was estimated to be 10^5 photons/mm^2/sec, and the typical exposure time was 10 minutes.*

Observation results of a sagittal slice of a rat cerebellar vermis are shown in Fig. 2-3; (a) is a phase-contrast X-ray image (interference pattern) and (b) is a corresponding absorption-contrast image. The latter image was obtained by blocking the reference beam with a lead plate. The exposure time was twice of that used to obtain the image (a). Figure 2-3(c) is a surface photograph of the sample, and Fig. 2-3(d) is a corresponding sketch. In the phase-contrast image (a), clear structure was revealed while no structure was observed in the absorption-contrast image (b). Comparing (a) with (c) and (d), one can see that

*The intensity loss due to the glasses supporting the sample was large. Later, by using a cell of plastic windows for sample holding, the exposure was shortened to be a few tens of seconds.

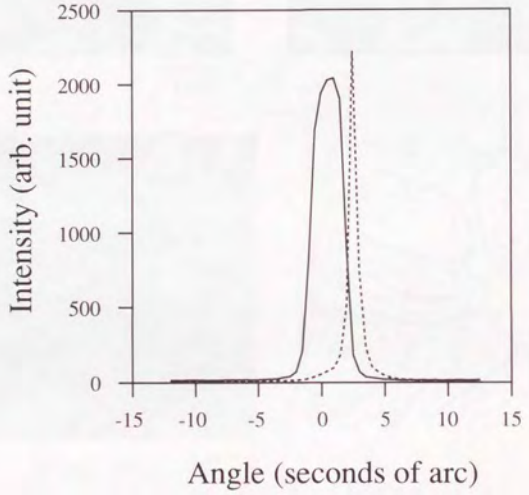

Fig. 2-2 Beam intensities of 1.0-Å X-rays (solid line) and the second harmonic (dashed line) outgoing from the interferometer measured simultaneously varying the incident angle of X-rays to the interferometer.

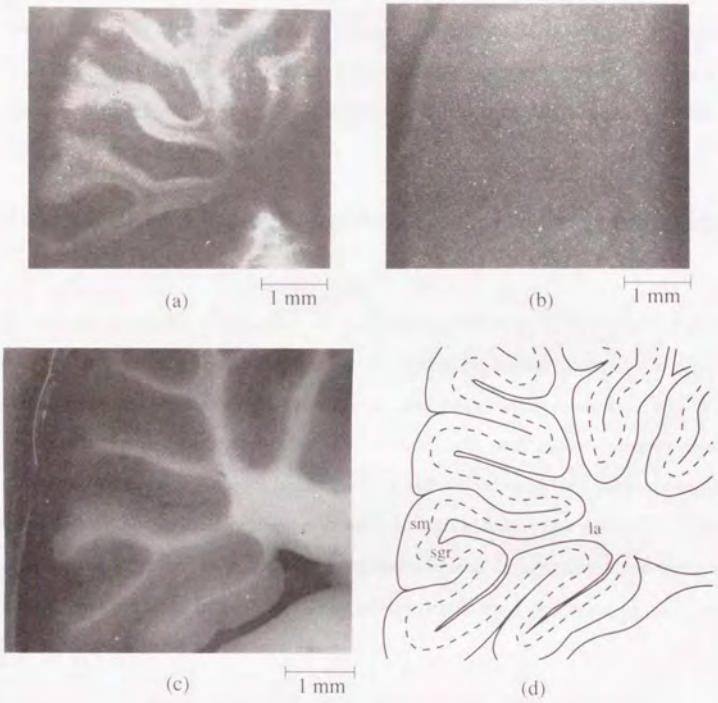

Fig. 2-3 X-ray interference pattern (a) and an X-ray absorption-contrast image (b) of an 1-mm sagittal slice of a rat cerebellum (vermis). The image (b) was obtained by blocking the reference beam with a lead plate. These images were recorded on X-ray films with 1-Å X-rays. The layer structure of the cerebellum was revealed in the image (a) while there was no clear structure in the image (b). An optical photograph (c) and a sketch (d) showed that the molecular layer (sm), granular layer (sgr), and white matter (la) were distinguished in the image (a).

white matter (la), granular layer (sgr), and molecular layer (sm) [17,18] were distinguished in the phase-contrast image. Distinction between the molecular layer and the granular layer in the phase-contrast image is clearer than in the optical photograph (c). Thus, it is evident that phase-contrast X-ray imaging is sufficiently sensitive to biological soft tissues.

2.3 Phase Determination from Interference Patterns

It must be noted that the creation of image contrast in Fig. 2-3(a) do not depend only on the structure inside the sample. If the slice happened to be a little thicker or thinner, the contrast would be different, and occasionally inverse. The image contrast varies depending on other optical condition, such as the inherent phase difference between the object beam and the reference beam that arises from the imperfection of the interferometer. If no information about the optical condition is known in advance, it is impossible to extract structural information from an interference pattern. In general, the interference pattern I produced by an object beam $A\exp(i\Phi)$ and a reference beam 1 is

$$\begin{aligned} I &= |1 + A\exp[i(\Phi + \Delta)]|^2 \\ &= 1 + A^2 + 2A\cos(\Phi + \Delta), \end{aligned} \tag{2.1}$$

where Δ is the inherent phase difference. The phase shift Φ conveys structural information of the object, and the determination of Φ leads us to quantitative understanding of the structure inside the object. One can determine $\cos(\Phi + \Delta)$ by measuring A by blocking the reference beam. Even if the Δ is known, however, calculating the arc cosine leaves uncertainty of $2\pi n$ (n: integer). In order to overcome this problem, the author has modified X-ray interferometry

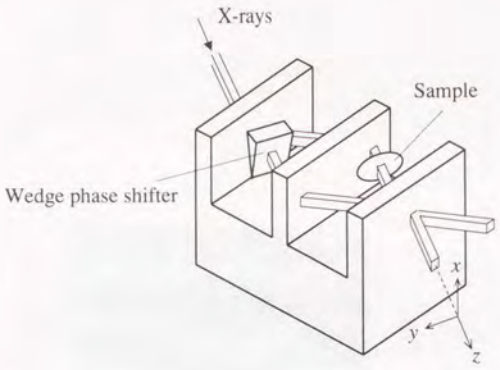

Fig. 2-4 A setting for the Fourier-transform method. The carrier fringes were produced by a wedge phase shifter placed in one of the beam paths.

to determine Φ definitively. Two techniques used alternatively in the modified X-ray interferometry are described below.

A. Fourier-Transform Method

The Fourier transform method [19] uses a wedge placed in the reference beam path as shown in Fig. 2-4. The wedge causes a uniform phase gradient, and produces interference fringes of a constant spacing called carrier fringes. When an object is placed in the object beam path, the carrier fringes bend due to the phase shift caused by the object, as illustrated in Fig. 2-5. The phase shift is proportional to the distance of the displacement of the carrier fringes. For example, the phase shift at the point P is $2\pi l/a$, where l is the distance of the fringe displacement and a is the spacing of the carrier fringes. Thus, one can determine Φ definitively from the interference pattern with the carrier fringes. The Fourier-transform method determines Φ using a computer with this concept.

Using the general expression of an interference pattern used in eq. (1.1), the

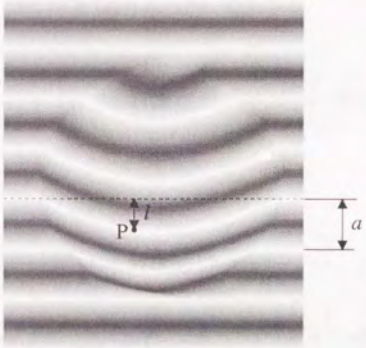

Fig. 2-5 An illustration of an interference pattern with the carrier fringes. When an object is placed in the view area, the carrier fringes bend due to the phase shift caused by the object. The phase shift is proportional to the distance of the fringe displacement. For example, the phase shift at the point P is $2\pi l/a$, where l is the distance of the fringe displacement at P and a is the carrier fringe spacing.

interference pattern $I(x,y)$ including the carrier fringes can be written as

$$I(x,y) = a(x,y) + b(x,y)\cos[2\pi f_o x + \Phi(x,y) + \Delta(x,y)], \tag{2.2}$$

where f_o is the reciprocal of the carrier fringe spacing (carrier frequency). The coordination is shown in Fig. 2-4. For explanation purposes, eq. (2.2) is rewritten as

$$I(x,y) = a(x,y) + c(x,y)\exp(2\pi i f_o x) + c^*(x,y)\exp(-2\pi i f_o x), \tag{2.3}$$

where

$$c(x,y) = \frac{1}{2}b(x,y)\exp[i\{\Phi(x,y) + \Delta(x,y)\}] \tag{2.4}$$

and * denotes the complex conjugate. The spectrum of spatial frequency in the x-direction is obtained by Fourier transforming $I(x,y)$ as

$$I_F(f,y) = a_F(f,y) + c_F(f - f_o, y) + c_F^*(f + f_o, y), \tag{2.5}$$

where the subscript F indicates the Fourier transform for each term in eq. (2.3). If the spatial variations of a, b, and Φ are slow compared to f_o, the peaks corresponding to the three terms in eq. (2.5) do not overlap. Therefore, the second or third term of eq. (2.5) that contains the information for the phase shift Φ is extracted separately. For example, let us extract the peak corresponding to the second term $c_F(f - f_o, y)$. By translating $c_F(f - f_o, y)$ by f_o along the frequency axis, $c_F(f,y)$ is obtained. This translation corresponds to cancellation of the phase gradient produced by the wedge. By extracting the peak corresponding to the third term, $c_F(f,y)$ is obtained as well. The inverse Fourier transform of

$c_F(f,y)$ with respect to f gives $c(x,y)$. The argument of the obtained $c(x,y)$ corresponds to $\Phi(x,y) + \Delta(x,y)$ (see eq. (2.4)). Because $\Delta(x,y)$ can be determined by analyzing the interference pattern in the absence of the object, a phase-mapping image $\Phi(x,y)$ is obtained by subtracting the $\Delta(x,y)$ measured in advance.

The calculation of the argument involves an operation of arc tangent. Therefore, the resultant value of Φ ranges between $-\pi$ and π. When the phase shift exceeds 2π, one sees phase jumps of 2π. Therefore, to obtain the true $\Phi(x,y)$, a phase unwrapping process is necessary. Because the Fourier-transform method assumes that the spatial variation of $\Phi(x,y)$ is slow, it is easy to compensate the phase jump (Fig. 2-6).

Figure 2-7 shows an example of the process of the Fourier-transform method. The sample was a slice from a human cancerous liver.† By Fourier transforming the interference pattern shown in Fig. 2-7(a) respect to x, three peaks corresponding to the terms in eq. (2.3) were obtained (Fig. 2-7(b)). Figure 2-7(c) was produced by choosing the left subpeak only and translating it to the origin. The inverse Fourier transform of Fig. 2-7(c) and the subsequent calculation of the argument produced the phase-mapping image $\Phi(x,y)$ (Fig. 2-7(d)).

The expected spatial resolution of the image obtained by using the Fourier-transform method is limited by the carrier fringe spacing, in the direction parallel to the x-axis. With the quality of the optics used in our measurements, the spacing of the carrier fringes available for observation was down to 0.05 mm. When narrower carrier fringes are used to obtain an image of a higher spatial resolution, the image processing was unsuccessful because fringe visibility got worse. In contrast, by using the fringe scanning method described next, the spatial resolution is theoretically the same as those of X-ray image sensors.

†Concentrating on the explanation of the method, the details of the sample and the image are not discussed here.

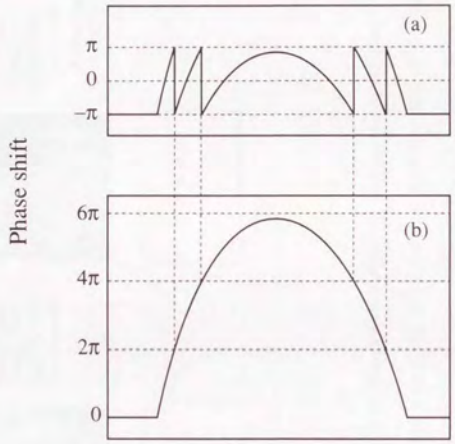

Fig. 2-6 The value of Φ ranges between -π and π because of the calculation of arc tangent in the argument extraction. Although the phase jumps of 2π occasionally appear, it is easy to compensate the jump if the spatial phase variation of the phase shift is not too steep.

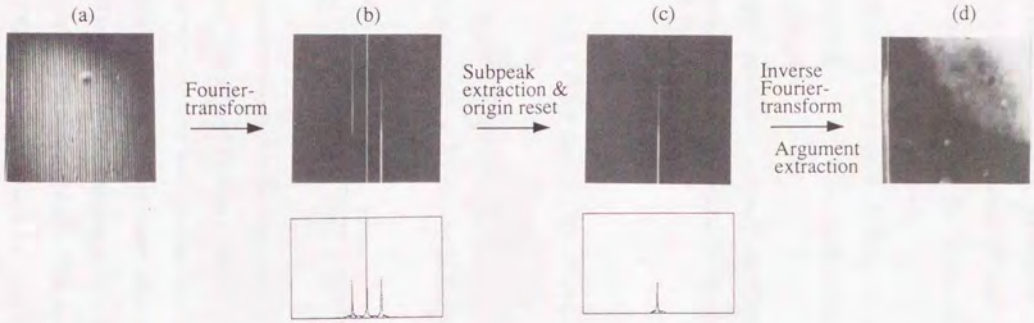

Fig. 2-7 Process of the Fourier-transform method. The Fourier-transform of the interference pattern (a) with the carrier fringes produced the image (b). The image (c) was produced by extracting the one of the subpeaks (in this case, the right subpeak) only and translating it to the origin. The inverse Fourier-transform of (c) and the subsequent calculation of the argument produced the phase-mapping image (d).

B. Fringe Scanning Method

The fringe scanning method [20] needs several interference patterns to produce one phase-mapping image Φ. When the relative phase difference between the object beam and the reference beam is changed, the interference fringes move depending on the amount of the phase change. The fringe scanning method determines $\Phi(x,y)$ by analyzing the relation between the movement and the given phase difference.

The fringe scanning method uses M interference patterns obtained by varying the relative phase difference at a $2\pi/M$ step. The interference patterns are written as

$$I(x,y;N) = a(x,y) + b(x,y)\cos\left(2\pi\frac{N}{M} + \Phi(x,y) + \Delta(x,y)\right), \qquad N = 1,2,\cdots,M. \tag{2.6}$$

Summation of $I(x,y;N)$ with weights of $\exp(-2\pi iN/M)$ yields

$$\sum_{N=1}^{M} I(x,y;N)\exp\left(-2\pi i\frac{N}{M}\right) = \frac{1}{2}Mb(x,y)\exp[i\{\Phi(x,y) + \Delta(x,y)\}]. \tag{2.7}$$

This equation shows that the argument of the summed up image equals $\Phi(x,y) + \Delta(x,y)$. The $\Delta(x,y)$ is determined in the absence of the object as well as in the Fourier-transform method, and thereby $\Phi(x,y)$ is obtained. The phase unwrapping process is also necessary after the calculation of the argument. The advantage of the fringe scanning method is that $\Phi(x,y)$ can be calculated independently at every point (x,y). This means that the spatial resolution of the phase-mapping image obtained by using the fringe scanning method is the same as that of the X-ray image sensor.

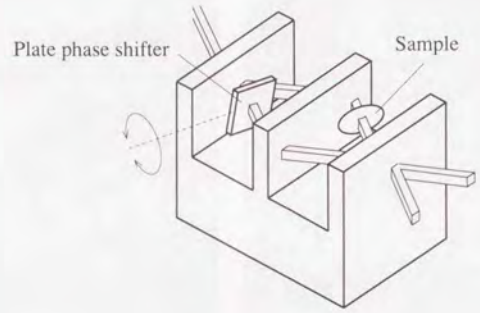

Fig. 2-8 A setting for the fringe scanning method. In this case, the phase difference was created and tuned by a plate phase shifter placed in one of the beam paths. By rotating the phase shifter, the effective thickness of the phase shifter was varied and the phase difference was tuned.

The phase difference can be created and tuned for example by moving the wedge in the direction corresponding to the wedge slope. Rotating a plate phase shifter is also practical, as shown in Fig. 2-8.

Figure 2-9 shows an example of the process of the fringe scanning method. The sample was an 1-mm-diameter plastic sphere in a cell filled with water.[‡] In this case, ten interference patterns (Fig. 2-9(a)) were taken, varying the phase difference by $2\pi/10$ per step with the plate phase shifter. Slight vertical stripes shown in Fig. 2-9(a) was due to the intensity nonuniformity in the incident X-ray beam to the interferometer. These stripes were independent of the X-ray phase, and therefore did not remain in the obtained phase-mapping image (Fig. 2-9(b)).

[‡]The detail of the cell will be described in Section 3.4.

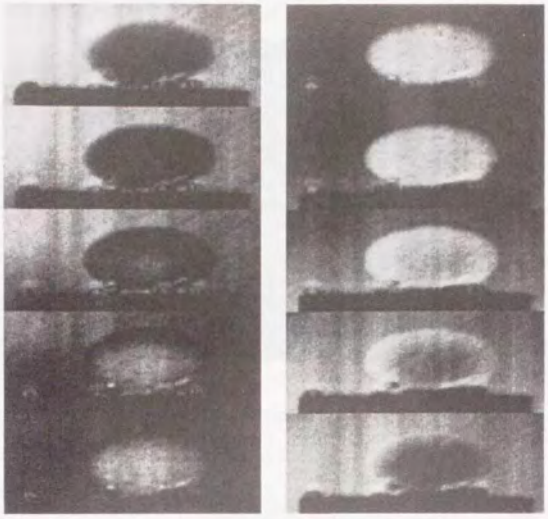

(a)

(b)

Fig. 2-9 Process of the fringe scanning method. The sample was an 1-mm-diameter plastic sphere. Ten interference patterns (a) were obtained by varying the phase difference at a $2\pi/10$ step. Calculating the argument of the data obtained by summing up the interference patterns with weights corresponding to the given phase differences, the phase-mapping image (b) was obtained. The magnification in horizontal and vertical directions differed.

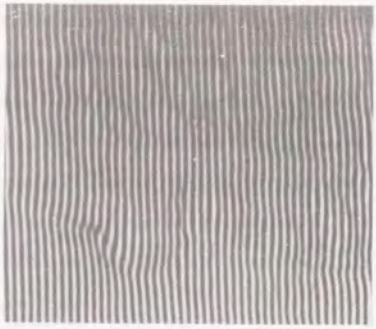

Fig. 2-10 An X-ray interference pattern of an 1-mm slice of a rat cerebellum with the carrier fringes.

2.4 Quantitative Analysis of X-Ray Phase Shift

In Fig. 2-3(a), the interference pattern corresponding to the layer structure of the rat cerebellum was presented. However, the origin of the image contrast was not clear. Therefore, phase-mapping images of the cerebellar slice were measured, and used to study the relation between the phase shift and the structures in the cerebellum. Assuming that the lipid distribution in the cerebellum played a dominant role to the contrast creation, the change in the X-ray phase shift due to lipid removal from the cerebellar slice was examined.

The Fourier-transform method was used in this experiment to obtain phase-mapping images. A wedge phase shifter made of acrylic resin was used. The carrier fringes with 120-μm intervals were produced for 0.92-Å X-rays. For computer image analysis, the interference pattern was obtained with an X-ray image sensor (X-ray sensing pickup tube [21] whose optimal spatial resolution was 8 μm). An 1-mm thick sagittal slice of a vermis was cut out from a rat cerebellum

fixed in formalin, which was a similar slice with the sample shown in Fig. 2-3. Figure 2-10 is an interference pattern of the slice with the carrier fringes.

Figure 2-11(a) is the phase-mapping image obtained by processing the interference pattern with the Fourier-transform method. Although the spatial resolution was worse than that in Fig. 2-3(a), the molecular layer, granular layer, and white matter were distinguished. The bright area corresponded to the granular layer. The molecular layer and white matter appeared dark. The relative phase shift on the line AB is shown in Fig. 2-11(b). It was found that the granular layer produced larger phase shift.

After the observation, the slice was processed for lipid removal. To remove lipid, the slice was dehydrated by ethanol and then sequentially put in xylene for 8 hours, in acetone for 12 hours, and in xylene for 7 hours [22]. After lipid was thus removed, the slice was immersed in ethanol and put back in formalin. The phase-mapping image measured after the lipid removal is shown in Fig. 2-11(c). The profile on the line AB is also shown in Fig. 2-11(d). Slight shrinkage of the slice was due to the lipid removal procedure.

As indicated by arrows in Figs. 2-11(c) and (d), the contrast of the white matter almost disappeared by the lipid removal. This means that lipid was replaced with water by the lipid removal procedure and that the the phase shift got near to that of the granular layer. This result is consistent in that the white matter contains higher percentage of lipid than other parts of a cerebellum [22]. Thus, it is clear that one of dominant origins of the phase-contrast creation is lipid in the cerebellum.

By analyzing the phase-mapping images, it was found that the X-ray phase shift was smaller when the concentration of lipid is larger. This means that the refractive index is smaller when lipid is contained more. This result cannot be obtained only by observing interference patterns because the phase shift cannot be analyzed quantitatively. Further discussion about this result from a histological

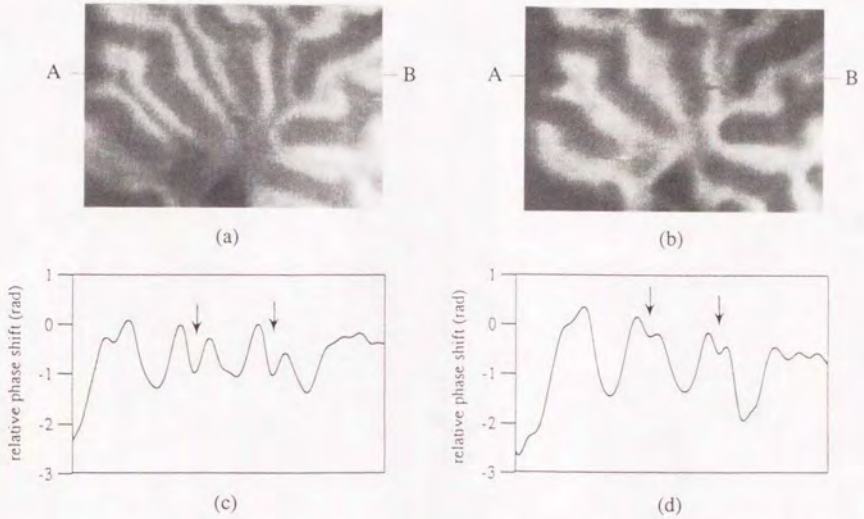

Fig. 2-11 Phase-mapping images of a rat cerebellar slice; (a) before and (b) after the lipid removal procedure. The relative phase shifts on the line AB are also shown; (c) before and (d) after the procedure. Contrast of the white matter indicated by arrows almost disappeared after the lipid removal. To obtain the phase-mapping images, the Fourier transform method was used.

aspect will be presented again in Section 4.4.

Chapter 3

Tomographic Image Reconstruction

3.1 Introduction

As the third step of phase-contrast X-ray imaging, the principle of phase-contrast X-ray CT is described in this chapter. The geometrical relation of phase-contrast X-ray CT among an object, an X-ray beam, and reconstructed images is the same as that of the conventional X-ray CT using absorption-contrast (Fig. 1-3). The image reconstruction algorithm of phase-contrast X-ray CT is also the same as that of conventional X-ray CT. The sole difference between phase-contrast X-ray CT and absorption-contrast X-ray CT is the input data to the reconstruction algorithm. Phase-contrast X-ray CT needs the phase-mapping images for the input data, while absorption-contrast X-ray CT needs the μt value which is calculated from the X-ray transmittance. Therefore, image sensitivities of the two methods are discussed by comparing the phase shift and μt at the atomic level. It is shown that phase-contrast X-ray CT is almost a thousand times more sensitive to light elements than the conventional method.

The phase-contrast X-ray CT system consists of an X-ray source, a monochromator, an X-ray interferometer, a sample holder, a phase shifter, an X-ray image sensor, and an image processing system. Most of the system is common to that

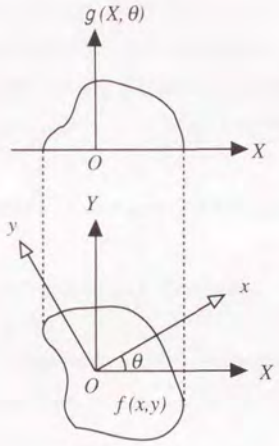

Fig. 3-1. The relation between the object $f(x,y)$ and the projection image $g(X,\theta)$.

shown in Figs. 2-5 and 2-8. For phase-contrast X-ray CT, the sample rotation holder was newly devised. A description of the details of the sample rotation holder and the design concept is included in this chapter.

3.2 Principle of Image Reconstruction

A two-dimensional coordinate system xOy fixed to an object is used to explain the principle of the image reconstruction (Fig. 3-1). Another coordinate system XOY that is fixed to the X-ray beam is also defined. These coordinates are inclined by θ each other, as shown in Fig. 3-1. The X-ray beam assumed to be parallel to the Y-axis. To acquire data for the CT image reconstruction, θ is changed by rotating the object or by rotating an X-ray source and an X-ray image sensor synchronously around the object.

Because the object has a three-dimensional structure, the third axis perpen-

dicular to the xOy plane must be taken into account. However, the principle of image reconstruction is explained for a two-dimensional case below because tomograms are reconstructed on the planes parallel to the xOy plane. A three-dimensional image can be created by stacking tomograms reconstructed on a series of planes parallel to the xOy plane.

In general, the input data g into a standard CT algorithm must have a form

$$g(X,\theta) = \int f(x,y)dY, \tag{3.1}$$

where f is a value that conveys structural information about the object. The CT image reconstruction means the determination of $f(x,y)$ from $g(X,\theta)$'s measured in different projection directions.

The reconstruction algorithm is based on Fourier transforms of the measured data. The Fourier transform of $f(x,y)$ is written as

$$F(\xi,\eta) = \int_{-\infty}^{\infty}\int_{-\infty}^{\infty} f(x,y)\exp[-i(\xi x+\eta y)]dxdy. \tag{3.2}$$

The expression of eq. (3.2) with a polar coordinate is

$$F(\omega\cos\theta,\omega\sin\theta) = \int_{-\infty}^{\infty}\int_{-\infty}^{\infty} f(x,y)\exp[-i\omega(x\cos\theta+y\sin\theta)]dxdy, \tag{3.3}$$

where

$$\xi = \omega\cos\theta \quad \text{and} \quad \eta = \omega\sin\theta. \tag{3.4}$$

Because

$$X = x\cos\theta + y\sin\theta \quad \text{and} \quad Y = -x\sin\theta + y\cos\theta, \tag{3.5}$$

eq. (3.3) is written as

$$F(\omega\cos\theta, \omega\sin\theta) = \int_{-\infty}^{\infty} g(X,\theta)\exp(-i\omega X)dX. \tag{3.6}$$

Thus, $F(\omega\cos\theta,\ \omega\sin\theta)$ is the Fourier-transform of the observed image $g(X,\theta)$ respect to X. The $f(x,y)$ is determined by inversely Fourier-transforming $F(\xi,\eta)$ as

$$f(x,y) = \frac{1}{4\pi^2}\int_{-\infty}^{\infty}\int_{-\infty}^{\infty} F(\xi,\eta)\exp[i(\xi x+\eta y)]d\xi d\eta. \tag{3.7}$$

Recently, fast Fourier transform (FFT) is easily used, and image reconstruction with this algorithm is practical.

However, because the F is measured on a polar coordinate system (ω,θ), one have to interpolate it into a rectangular coordinate system (ξ,η) to use eq. (3.7). The interpolation must be started after all projection data are acquired. This demand prevents us from starting the reconstruction process during the CT scan.

For quicker image reconstruction, the filtered back-projection method and the convolution method described below are used. The both methods are mathematically equivalent to the above method based on Fourier transform, and enable us to start image reconstruction before the CT scan ends.

Using a polar coordinate system, eq. (3.7) is written as

$$f(x,y) = \frac{1}{8\pi^2}\int_0^{2\pi}\left[\int_{-\infty}^{\infty} F(\omega\cos\theta,\omega\sin\theta)|\omega|\exp(i\omega X)d\omega\right]d\theta. \tag{3.8}$$

The integral in the [ ] of the above equation corresponds to the modification of $F(\omega\cos\theta,\omega\sin\theta)$ with a filter function $|\omega|$ in the space of the spatial frequency. Eq. (3.8), therefore, means that $f(x,y)$ can be determined by back-projecting the modified projection data. The method that uses eq. (3.8) is thereby called the filtered back-projection method.

The advantage of this method is that CT image reconstruction can be started just after the first projection data is measured because F's on the polar coordinate system can be used to calculate $f(x, y)$. However, a divergent function $|\omega|$ in eq. (3.8) is not appropriate to actual calculation. Instead, a modified filter function that is not divergent are usually used. The simplest modified filter function $H(\omega)$ is [23]

$$H(\omega) = \begin{cases} |\omega| & (\omega \leq W) \\ 0 & (\omega > W) \end{cases} \tag{3.9}$$

where W is the maximum frequency determined by the pixel size of the X-ray image sensor employed for measurements.

The Fourier transform with a filter function can be rewritten to a convolution form. Therefore,

$$f(x, y) = \frac{1}{4\pi} \int_0^{2\pi} \left[\int_{-\infty}^{\infty} g(X', \theta) h(X - X') dX' \right] d\theta, \tag{3.10}$$

is equivalent to eq. (3.8), where the convolution function $h(X)$ is the inverse Fourier transform of the filter function $H(\omega)$. In this study, this convolution method was used, using the convolution function that was the inverse Fourier-transform of $H(\omega)$ in eq. (3.9).

3.3 Quantity Revealed by Phase-Contrast X-Ray CT

In the conventional X-ray CT, the f in eq. (3.1) corresponds to the linear absorption coefficient μ, and the projection is

$$\int \mu dY = -\log T \equiv \mu t, \tag{3.11}$$

where T is the X-ray transmittance of the object. Therefore, by measuring the X-ray transmittances in different projection directions and by calculating the logarithms of them, input data to the CT reconstruction algorithm are prepared. Consequently, tomograms that reveal the distribution of μ are obtained.

On the other hand, the projection relation

$$\frac{2\pi}{\lambda}\int \delta dY = \Phi \tag{3.12}$$

is found in the X-ray phase shift process, where λ is the X-ray wavelength and δ is the refractive index decrement from unity. Thus, the form of this equation satisfies eq. (3.1), and tomographic image reconstruction using Φ as the input data is achieved with a standard algorithm. Phase-contrast X-ray CT thereby depicts the distribution of δ inside the object by processing Φ's obtained in different projection directions. Interference patterns do not have a projective form (see eq. (2.1)), and therefore cannot be processed under a tomographic configuration. Thus, measuring phase-mapping images Φ is indispensable to achieve phase-contrast X-ray CT.

The difference between phase-contrast X-ray CT and absorption-contrast X-ray CT is thus their input data to the reconstruction algorithm—Φ and μt. Here, to compare image sensitivities, the magnitudes of Φ and μt per atom are compared. Using the atomic absorption coefficient μ_a, eq. (3.11) is written as

$$\mu t = \int \sum_k N_k \mu_{ak} dY, \tag{3.13}$$

where N_k is the atomic density of element k. On the other hand, δ in eq. (3.12) is written as [24]

$$\delta = \frac{r_e \lambda^2}{2\pi} \sum_k N_k (Z_k + f_k'), \tag{3.14}$$

where Z, f^r, and r_e are the atomic number, the real part of the anomalous atomic scattering factor, and the classical electron radius. The substitution of eq. (3.14) into eq. (3.12) yields

$$\Phi = \int \sum_k N_k p_k dY, \quad p_k \equiv r_e \lambda (Z_k + f_k^r). \tag{3.15}$$

Thus, the difference between eqs. (3.13) and (3.15) is μ_a and p. Therefore, the image sensitivities for the absorption-contrast method and the phase-contrast method are compared by calculating μ_a and p.

The both values can be calculated using the data reported in refs. [25,26]. In Fig. 3-2, p and μ_a are plotted versus the atomic number. The curves for 1.5-Å, 0.92-Å, 0.5-Å and 0.2-Å X-rays are shown. It is easy to see that p is always greater than μ_a. The difference extends to about a thousand times for light elements. This means that the phase-contrast method is much more sensitive to light elements than the absorption-contrast method.

But image contrasts produced by p and μ_a are different because p and μ_a depend on the atomic number in different manners. Therefore, the image sensitivities must be discussed carefully when the composition is not uniform. However, assuming that the composition inside an object is almost uniform and that only the density is different, image contrasts produced from the distributions of Φ and μt are the same. Then, the difference between Φ and μt coincides with the sensitivity difference. In fact, biological soft tissues consists of mainly hydrogen, carbon, oxygen and nitrogen, and the composition can be assumed to be almost uniform. Consequently, it is concluded that the image sensitivity of phase-contrast X-ray CT to biological soft tissues is approximately a thousand times greater than that of absorption-contrast X-ray CT.

The detection accuracies of Φ and μt must be also discussed for the image comparison. According to the fringe scanning method, the determination error

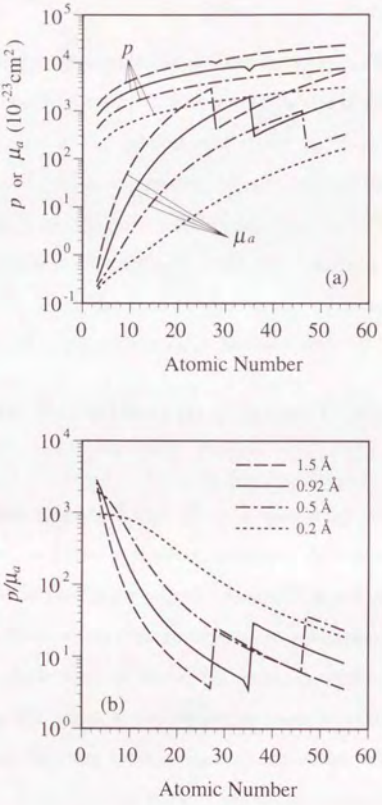

Fig. 3-2 Calculated value of p and μ_a (a) and the ratio p/μ_a (b) versus the atomic number plotted for X-rays of 0.2, 0.5, 0.92, and 1.5 Å.

in the phase shift $\Delta\Phi$ is

$$\Delta\Phi = \frac{1}{\sqrt{N_p}}, \tag{3.16}$$

where N_p is the total interfering photon number detected during the fringe scan [27]. As to the Fourier-transform method, the accuracy is also at almost the same level, assuming the estimation at the same spatial resolution. It is easy to see that the determination error of μt is also equal to the reciprocal of the square root of the number of detected X-ray photons. Therefore, it is concluded that there is no difference in the signal-to-noise ratio of the images mapping Φ and μt under the same X-ray exposure. Thus, the above estimation of the image sensitivity is true even when the detection accuracy is taken into account.

3.4 Sample Rotation in Phase-Contrast X-Ray CT

As mentioned, phase-contrast X-ray CT is achieved by measuring the phase-mapping images from different projection directions. In this study, the projection direction was varied by rotating a sample because X-rays from a SR source were used. This section describes the design concept of a rotation stage for a sample.

The optics for phase-contrast X-ray CT is fundamentally the same as Fig. 2-4 or Fig. 2-8. For CT scans, a mechanism for sample rotation must be added. First, it is explained that the rotation axis of the sample should be parallel to the scattering plane of the interferometer—the plane containing the object beam path and the reference beam path.

This is because visibilities of fringes parallel to and perpendicular to the scattering plane are different. The anisotropy of the fringe visibility was revealed in the interference pattern of a plastic sphere shown in Fig. 3-3. In this case, a wedge phase shifter was placed in the reference beam path. Horizontal fringes

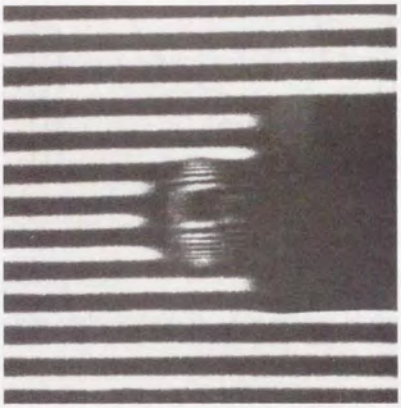

Fig. 3-3 An X-ray interference pattern of a plastic sphere exposed to air. The interference fringes near the left and right sides in the image of the sphere disappeared. The horizontal fringes in the background were the carrier fringes. The dark area on the right side of the sphere was the shadow of the rod supporting the sphere.

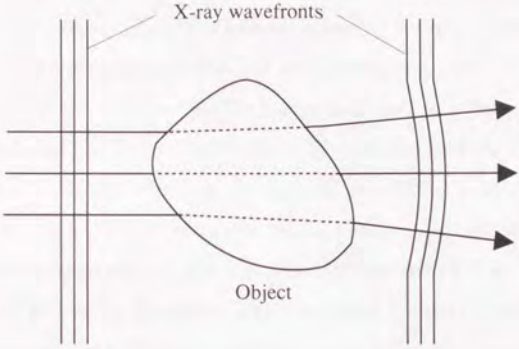

Fig. 3-4 Illustration of the beam deflection due to the refraction by an object. For comprehensiveness, the beam deflection is illustrated exaggeratedly. The deflection angle is typically a few seconds of arc.

in the background were the carrier fringes produced by the phase shifter. Fine fringes at the center of the picture were produced by the sphere, and the dark area in the right of the image was the shadow of the holder rod of the sphere. If the fringe visibility was isotropic, circle fringes should be shown. However, fringes at the left and right sides of the sphere were not shown, while fine fringes were shown in upper and lower parts of the sphere. This means that the visibility of vertical fringes was relatively low especially when the spacing was narrow, and that the fringes at the left and right sides of the sphere were smeared out.

This phenomenon is related to the performance of the three slabs of the interferometer. In Section 1.2, it was explained that the crystal slabs function as X-ray half-mirrors. Strictly, the performance is influenced by the incident angle of the X-rays. As a matter of fact, X-ray beam is deflected by the object due to refraction, as illustrated in Fig. 3-4. The refractive index of organic materials

for X-rays is typically $1 - 10^{-6}$ and the deflection angle is occasionally as large as several seconds of arc. Usually this beam deflection is negligible assuming the observation with the spatial resolution of several tens of microns. Actually, the principle of X-ray CT assumes that the X-rays propagate in a straight line.

However, when the X-ray interferometer is used, the amount of the beam deflection is not negligible because the angular width that satisfies the Bragg diffraction condition of the analyzer (the third slab) is one or two seconds of arc. Therefore, the incident angle of the object beam to the analyzer cannot assumed to be uniform within the view area. X-rays deflected beyond the angular width cannot pass the analyzer. Consequently, interference fringes do not appear. Even when the deflection angle is within the angular width, the fringe visibility is influenced.

The dynamical theory of X-ray diffraction by a perfect crystal shows that the deflection of the incident X-rays from the exact Bragg angle causes much larger deflection of the direction of the X-ray propagation in the crystal [16,28], as illustrated in Fig. 3-5. Roughly estimated, the beam deflection angle is magnified by 10^4 times in a crystal. This means that the exit of the deflected beam behind the third slab is considerably different from that of the beam at the exact Bragg condition. Then, the spatial coherency between the object beam and the reference beam, which is on the exact Bragg diffraction condition, is insufficient. Consequently, the fringe visibility decreases.

However, when the incident beam deflects in the perpendicular direction to the diffraction vector H shown in Fig. 3-5, the Bragg diffraction condition is not influenced. Therefore, the beam deflection in this direction do not cause the magnification of the beam deflection in the crystal. The anisotropy of the fringe visibility arose from this anisotropic response of the X-ray half-mirror to the deflection of the incident beam.

Hence, the rotation axis of the sample parallel to the scattering plane was

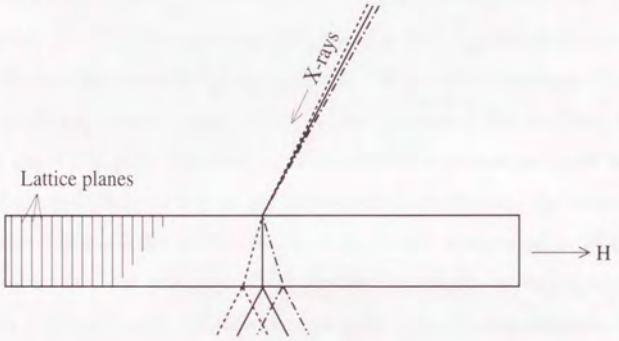

Fig. 3-5 X-ray beam path in the crystal varies sensitively depending on the incident angle. A few seconds of deviation in the incident angle in the parallel direction to the diffraction vector H causes a few degrees of beam deflection in the crystal. Consequently, the exit point of X-rays varies remarkably depending on the incident angle. When the incident beam deflects in the perpendicular direction, such a phenomenon does not occur.

adopted for CT scans. In this case, the CT reconstruction concerns to the phase-shift profile in the vertical direction. The fringe visibility is highest in this direction.

Apart from the fringe visibility discussed above, however, it is hard to determine the phase-mapping image from an interference pattern such as Fig. 3-3, where interference fringes are too narrow. The spatial resolution of the X-ray image sensor available for digital image processing is limited to about ten microns at present. Therefore, it is preferable to observe objects that do not produce narrower fringes than the detector resolution limit. But this does not mean that only small or thin objects are observable with this technique. The narrower fringes means larger deflection by refraction. Large refraction occurs mainly at the surface of the sample when the sample is observed in air because the jump of the refractive index is large at the surface. If the sample is observed in liquid, too large refraction does not occur at the surface because the difference in the refractive indices of liquid and the sample is suitably small. Consequently, fringes due to outline shape is adequately controlled. Figure 3-6 shows the interference pattern produced by the plastic sphere immersed in water. The spacing of the fringes was reasonable for the image processing.

To observe the image in Fig. 3-6, a cell filled with water was used, and the structure is shown in Fig. 3-7. On the entrance and exit sides of X-rays, thin plastic plates were attached on the cell frame. They were parallel, and no beam deflection occurred at the window by aligning the cell so that the X-ray beam impinged on the window from the normal direction. The horizontal rod for the rotation of the sample pierced a hole prepared on the cell frame. The frame was fixed to the rigid part of the apparatus, and thereby only the sample could rotate against the X-ray beam.

Moreover, the cell is convenient for the observation of biological soft tissues, which are usually wet. If necessary, the refractive index of the liquid in the cell

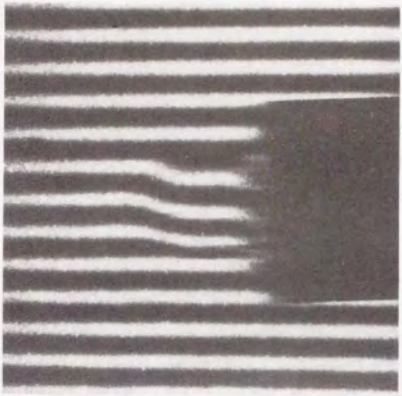

Fig. 3-6 An X-ray interference pattern of the plastic sphere in water. Interference fringes were visible throughout the area in view.

can be adjusted to almost the same value as the average refractive index of the sample by mixing other solution in water, aiming at the reduction of the beam deflection at the sample surface more effectively. Furthermore, the physiological environment can be controlled when biological tissues are observed.

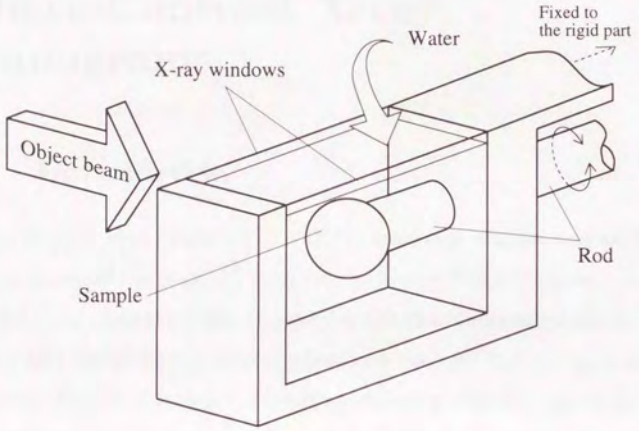

Fig. 3-7 The structure of a sample cell filled with water. A sample was attached to a rod and rotated in the cell. The frame of the cell was fixed to the other part of the apparatus, and only the sample rotated against the object beam. X-ray windows made of plastic plate were attached at the entrance and exit sides of the cell.

Chapter 4

Phase-Contrast X-ray Tomograms

4.1 Introduction

In this chapter, observation results with the apparatus of phase-contrast X-ray CT are presented. In Section 2.3, two methods—the Fourier-transform method and the fringe scanning method—were described for obtaining phase-mapping images from interference patterns, which were used for the CT image reconstruction. First, it is shown that the fringe scanning method is appropriate for phase-contrast X-ray CT by comparing the tomograms of a plastic sphere reconstructed from phase-mapping images obtained with the two methods. Next, ring artifacts characteristic of phase-contrast X-ray CT are discussed. The origin of the artifacts and measures to reduce the artifacts are described.

The phase-contrast X-ray CT apparatus improved to reduce the artifacts was applied to the observation of cancerous tissue. The purpose of that observation was to examine whether phase-contrast X-ray CT distinguishes cancer lesions from normal tissue without staining, aiming at medical applications. Although the observation area is limited to 5 mm at present, a three-dimensional image that reveals cancerous parts is presented.

In addition to obtaining image contrast, another important task in diagnostic

X-ray imaging is to understand the image contrast in relation to the structure. In the case of phase-contrast X-ray CT, what information is obtained from tomograms? Section 3.3 showed that the distribution of δ creates the image contrast of phase-contrast tomograms. In Section 4.4, more detailed discussion about the meaning of the image contrast of phase-contrast tomograms is presented. Based on the discussion, the contrast effect of human blood is considered, as an example of another possible observation target with the phase-contrast technique in biological systems.

The present technique involves unsolved problems, particularly for medical application. Finally, problems are pointed out, and a strategy for application of phase-contrast X-ray imaging are briefly discussed.

4.2 Preliminary Studies Using Test Object

This section first compares the phase-contrast tomograms obtained with the Fourier-transform method and with the fringe scanning method using a plastic sphere 1 mm in diameter as a test sample. The plastic is a compound of polymethylmethacrylate and polystyrene. To create the carrier fringes for the Fourier-transform method, a 45° wedge-shaped phase shifter made of acrylic resin was used. This phase shifter produced carrier fringes with 78.5-μm intervals for 0.92-Å X-rays. The sample was rotated in 1.8° steps in the cell filled with water (Fig. 3-8). For the convenience of the experiments, the same phase shifter was used to apply the fringe scanning method. The wedge was moved in the direction of the wedge slope; the thickness varied and the phase difference was proportional to the distance of the wedge displacement. Four interference patterns were measured to obtain a phase-mapping image by moving the wedge in steps of one quarter of the carrier fringe spacing.

The phase-contrast tomograms obtained with the Fourier-transform and fringe

scanning methods are shown in Figs. 4-1 and 4-2. Tomograms are presented for three slice locations. The slice 1 corresponds to the center of the sphere. The interval between the slice locations was 175 μm. The thickness of the slices corresponded to 35.1-μm. The tomograms were reconstructed by 512 $\times$ 512 pixels, and the pixel size was 5.7 μm $\times$ 5.7 μm. Comparing the phase-contrast tomograms obtained with these methods reveals two characteristic differences.

One is that the spatial resolution of the phase-contrast tomograms obtained with the fringe scanning method (Fig. 4-2) is better than that of tomograms obtained with the Fourier-transform method (Fig. 4-1). The spatial resolution of the tomograms in Fig. 4-1 is estimated to be 120 μm from the edge steepness in the sample image, and the value is almost the same as the theoretically calculated resolution limit for the Fourier-transform method (Section 2.3). On the other hand, it is easy to see that the spatial resolution of the tomograms in Fig. 4-2 is much better. Small bubbles accidentally mixed in during molding are resolved (dark dots). Estimating from the size of detected bubbles, the spatial resolution is less than 40 μm. This result is consistent with the theoretical prediction that the fringe scanning method provides phase-mapping images of the spatial resolution better than that achieved with the Fourier-transform method.

The other difference is that there are ring artifacts in the phase-contrast tomograms obtained with the fringe-scanning method (Fig. 4-2). In this case, the phase drift was responsible for the artifacts, as verified by the experimental results described below.

When the beam intensity outgoing from the interferometer was monitored with a NaI scintillation detector through a 0.3 mm $\times$ 0.3 mm slit, the intensity fluctuated randomly on the time scale of seconds (Fig. 4-3(a)). It was clear that this phenomenon was not the result of a fluctuation in beam intensity itself, but rather arose from the movement of the interference fringes across the view area. This is because the beam intensity measured by the NaI scintillation

Slice 1 Slice 2 Slice 3

Fig. 4-1 Phase-contrast tomograms of the plastic sphere 1 mm in diameter obtained with 0.92-Å X-rays. These tomograms were reconstructed from the phase-mapping images produced by the Fourier-transform method. Slice 1 corresponds to the center of the sphere.

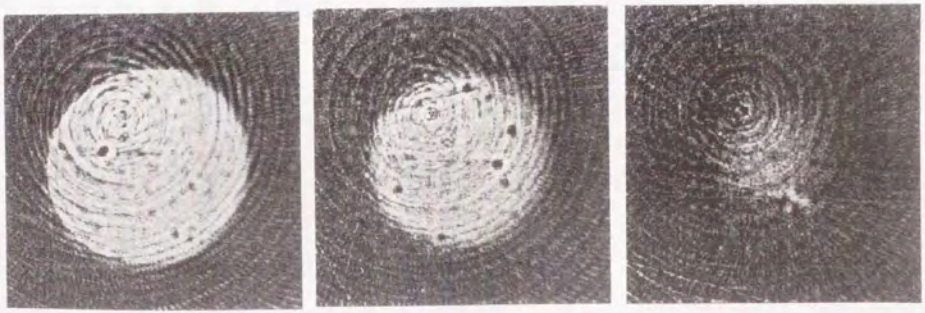

Slice 1 Slice 2 Slice 3

Fig. 4-2 Phase-contrast tomograms of the plastic sphere 1 mm in diameter obtained with 0.92-Å X-rays. These tomograms were reconstructed from the phase-mapping images produced by the fringe scanning method. Slice 1 corresponds to the center of the sphere. Dark dots shown in the tomograms are bubbles accidentally mixed in during molding.

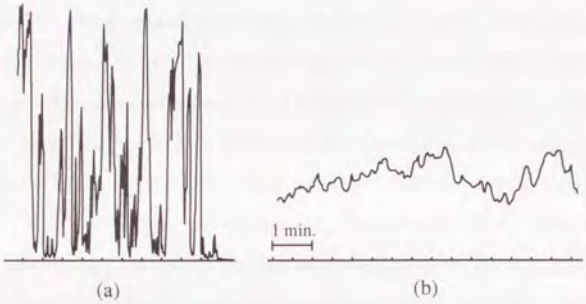

Fig. 4-3 Intensity of the beam outgoing from the interferometer monitored with a NaI scintillation detector through a 0.3 mm × 0.3 mm slit. The fluctuation in the monitored intensity decreased from (a) to (b) by covering the interferometer with a hood.

detector became stable when the propagation of the reference beam was interrupted. Therefore, it is likely that the interference pattern moved during the beam exposure and image acquisition in our experiments of phase-contrast X-ray CT. The movement of the interference pattern means that the phase difference between the two beams was not kept stable. Because the fringe scanning method assumes that the phase difference is varied at a constant step, the movement of the interference pattern, or the phase drift, must cause errors in the determination of phase-mapping images. Actually, the carrier fringes slightly remained being superposed on the phase-mapping images when the interference fringes moved during the fringe scan. The remaining fringes were responsible for the ring artifacts in the tomograms. On the other hand, such ring artifacts do not appear in the tomograms obtained with the Fourier-transform method because a phase-mapping image is produced from one interference pattern.

Thus, the fringe scanning method provided better spatial resolution, but the image quality was degraded by the ring artifacts. Which method is appropriate for phase-contrast X-ray CT? As mentioned, the spatial resolution achieved by the Fourier-transform method is limited by the carrier fringe spacing. Therefore, to improve the spatial resolution, a wedge phase shifter that produces finer carrier fringes must be used. However, using our experimental setup, fringe visibility decreased when the fringe spacing was less than 50 μm. Then, the conversion from an interference pattern to a phase-mapping image will be not accurate. On the other hand, the spatial resolution at the same level as that of the image sensor is achieved in principle by using the fringe scanning method. Therefore, the fringe scanning method was adopted for the observation shown later. Instead, efforts were made to reduce the phase drift, as described below.

First, the interferometer was covered with a hood, and the intensity of the X-ray beam outgoing from the interferometer was monitored. As shown in Fig. 4-3(b), the hood was evidently effective to reduce the fluctuation in the beam intensity. This suggests that the air flow around the interferometer caused the movement of the interference pattern. It is likely that the temperature gradient caused by the air flow was responsible for deformation of the interferometer. The movement of the fringes, or the phase drift, must arose from the deformation.

Furthermore, the wedge phase shifter was replaced with a plate phase shifter. By rotating the plate phase shifter, the effective thickness varies and the phase difference can be tuned. The advantage of this phase shifter is that no carrier fringe is produced. Therefore, even if the phase difference drifts to some extent, no stripe pattern appears on phase-mapping images. Consequently, the ring artifacts do not appear. Instead, the rotation angle of the plate phase shifter is nonlinear to the produced phase difference and must be calibrated in advance.

The X-ray wavelength was also changed to 0.7 Å. The advantages of using shorter wavelength are that the attenuation in the beam intensity by passing

through the sample (and the cell filled with water) is smaller, and that the spacing of the interference fringes is wider because the phase shift is proportional to the wavelength (see eqs. (3.12) and (3.14)). Therefore, our experimental station was also moved to BL-14B, where high-flux X-rays of this wavelength were available from the vertical wiggler. Because the X-rays were linearly polarized in vertical direction there, moreover, the intensity loss due to polarization was avoided. The X-ray flux in front of the sample was estimated to be 5×10^5 photons/mm^2/sec.

The improved experimental setup is shown in Fig. 4-4. Figure 4-5 shows a detailed view of the apparatus of phase-contrast X-ray CT. The X-ray interferometer was placed on a table of the goniometer whose rotation accuracy was 0.01". The stages of the sample and the phase shifter were fixed on a base. The base was isolated from the goniometer for the interferometer to prevent vibration caused by fringe scans and CT scans from disturbing interference. The designs of the stages of the sample and the phase shifter were almost the same. Each stage consisted of horizontal and vertical linear stages and a rotation stage of a horizontal axis. The displacement of the sample rotation axis was designed within 2 μm over 360° rotation. All translations and rotations were controlled by pulse motors. The interferometer was covered with a hood for reduction of the phase fluctuation. On all sides of the hood, polymer sheets were attached. Because holes for the insertion of the sample and the phase shifter were prepared, the effect of the hood was insufficient. Therefore, the larger hood that covered the whole space on the base was also used. The walls of the hood were made of acrylic resin. X-ray beams passed through the holes made on the walls, where polymer films were attached. Figure 4-6 is pictures of the apparatus. By using this apparatus, the X-ray interferometer was stable for more than several hours.

An example of the phase-mapping image obtained with this apparatus has already been presented in Fig. 2-9. In this case, the X-ray image sensor was operated at a pixel size of 6 μm $\times$ 12 μm. Using such phase-mapping images,

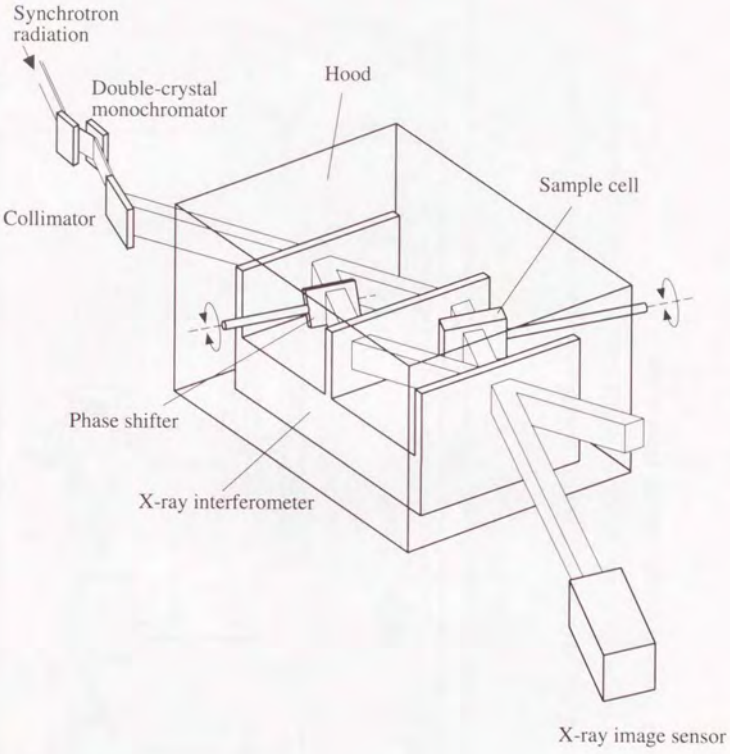

Fig. 4-4 Experimental setup of phase-contrast X-ray CT. The phase difference between the two beams was varied and tuned by rotating a plastic phase shifter. The interferometer was covered with a hood to reduce the phase drift. The collimator was used to expand the beam size in this case.

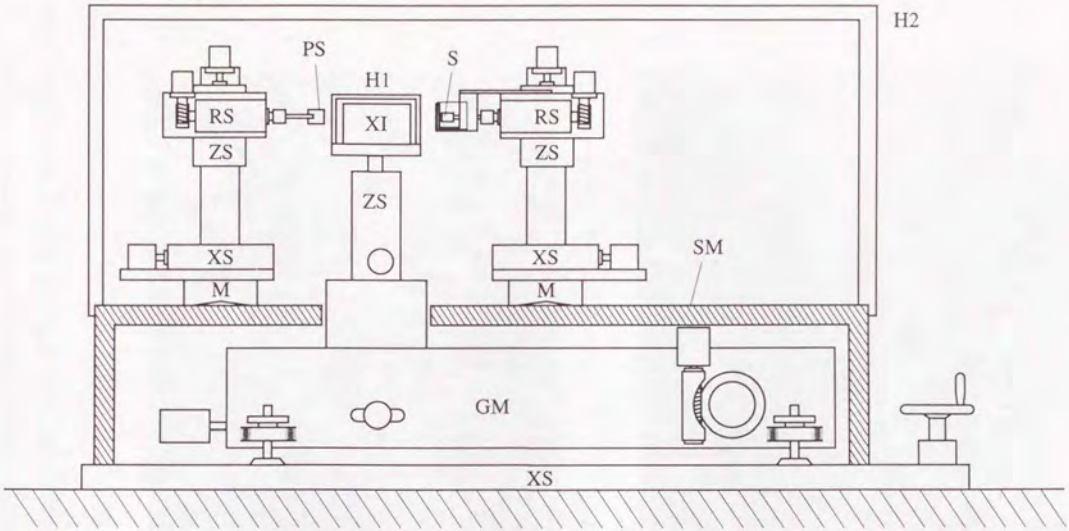

Fig. 4-5 A view of the apparatus of phase-contrast X-ray CT from the downstream of the X-ray beam. XI: X-ray interferometer, GM: goniometer for the interferometer, XS: horizontal linear stage, ZS: vertical linear stage, RS: rotation stage, SM: base, H1 and H2: hoods, S: sample, and PS: phase shifter.

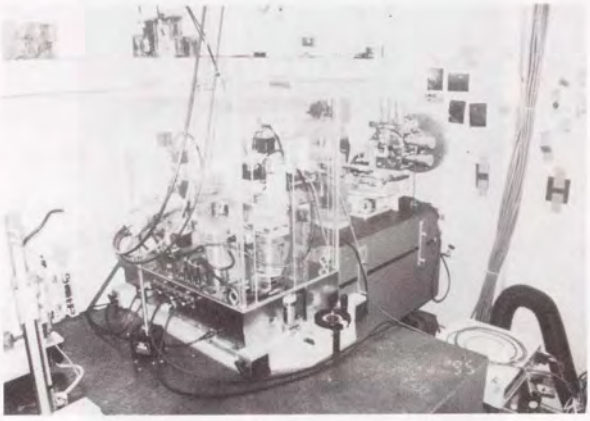

(a)

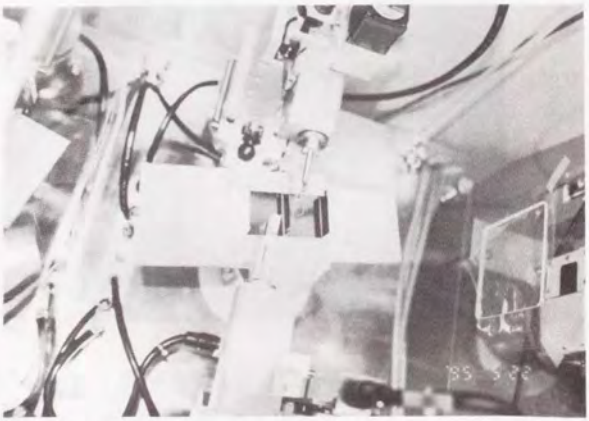

(b)

Fig. 4-6 Pictures of the apparatus of phase-contrast X-ray CT. (a) The whole view. (b) The view around the interferometer (the hood has been removed).

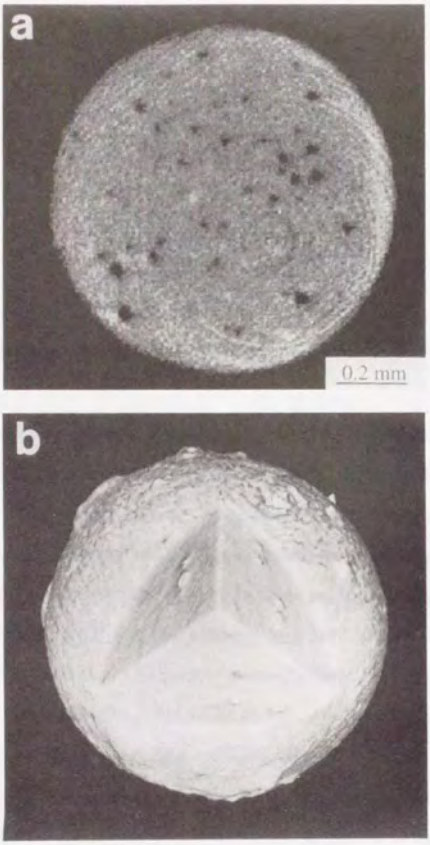

Fig. 4-7 Phase-contrast tomogram of the plastic sphere 1 mm in diameter. (a) One of the reconstructed tomogram. The thickness corresponding to the tomogram is 12 μm. Dark dots shown in the image are bubbles accidentally mixed in during molding. (b) A three-dimensional expression of the entire data made by stacking all tomograms. One octant has been cropped to show the inside of the sphere.

Fig. 4-8 Absorption-contrast tomogram of the plastic sphere.

the reconstructed phase-contrast tomogram of the plastic sphere is shown in Fig. 4-7. A tomogram near the center of the sphere is shown in (a). The thickness of the tomogram corresponds to 12 μm. The three-dimensional expression of the entire data made by stacking all tomograms is shown in (b). One octant has been cropped to show the inside of the sphere. In this case, phase-mapping images were measured at two hundreds angular settings over 180°. Assuming that the X-ray beam propagates in a straight line, measurements from 180° to 360° were omitted. The tomograms were reconstructed using the convolution backprojection method described in Section 3.2. The ring artifacts were thus much less than those in Fig. 4-2. The spatial resolution was also improved, and the bubbles are detected a little more clearly. The resolution limit of the system is estimated to be about 30 μm.

Finally, phase-contrast and absorption-contrast tomograms were compared. Figure 4-8 shows an absorption-contrast tomogram of the plastic sphere obtained by interrupting the propagation of the reference beam. The wavelength and flux of the X-rays irradiated to the sample were the same as those used to obtain the phase-contrast tomograms. The high sensitivity of phase-contrast X-ray CT is

readily evident.

4.3 Application to Biological System

The motivation of the development of this technique is the observation of biological soft tissues. Here, an observation result of a cancerous rabbit liver fixed in formalin is presented. VX2 cancer cells were implanted in a rabbit to generate the cancerous liver. The liver was removed two months later and fixed in formalin. A cylindrical piece, approximately 5 mm in diameter, was removed for CT observation. The sample was set in the water-filled cell (Fig. 3-7). The phase-mapping images were acquired by rotating the sample in 0.9° steps over a scan of 180°. A ten-step fringe scan was made at every angular setting. Assuming that the X-ray beam propagates in a straight line, measurements from 180° to 360° were omitted. Interference patterns were measured with the X-ray image sensor operating at a pixel size of 12 μm $\times$ 12 μm. Tomograms were reconstructed using the convolution-backprojection method with 512 $\times$ 512 pixels. Stacking tomograms, a three-dimensional image of 12 μm^3 voxels was obtained.

One of the reconstructed tomograms is shown in Fig. 4-9(a) and a three-dimensional expression of the entire data made by stacking all tomograms is shown in Fig. 4-9(b), where one quadrant and outer part have been cropped. Fig. 4-9(c) is an optical photograph of the specimen which was cut into a 10 μm slice and stained with haematoxylin-eosine after the X-ray observation. The slice position corresponds to that shown in (a). Comparing (a) with (c), one can see that the cancer lesion (left half) is easily distinguishable from the normal liver tissue (right half) and, moreover, that the structure inside the tumor is made visible. Two characteristic areas of bright and dark contrast exist in the tumor. The bright area is identified as a degenerated cancer lesion, and the dark as nondegenerated. Fibrous structures are also depicted in the marginal region

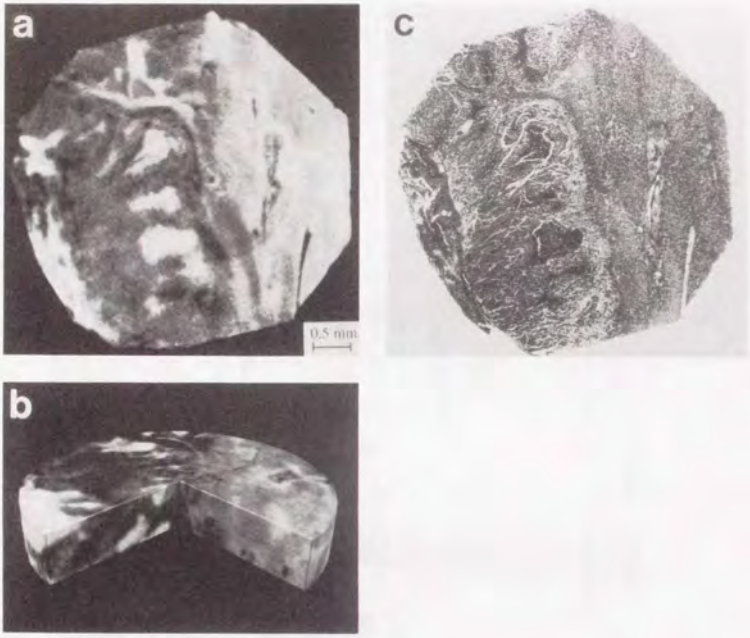

Fig. 4-9 Phase-contrast tomogram of a sample cut from a cancerous rabbit liver fixed in formalin. (a) One of the reconstructed tomograms. The thickness corresponding to the image is 12 μm. (b) A three-dimensional expression of the entire data made by stacking all tomograms. One quadrant and outer part have been cropped. (c) An optical photograph of the specimen which was cut into a 10 μm slice and stained with haematoxylin-eosine after the X-ray observation. The slice position of the specimen corresponds to that shown in (a). The cancer lesion (left half) is easily distinguishable from the normal liver tissue (right half). Structures in the tumor are also shown.

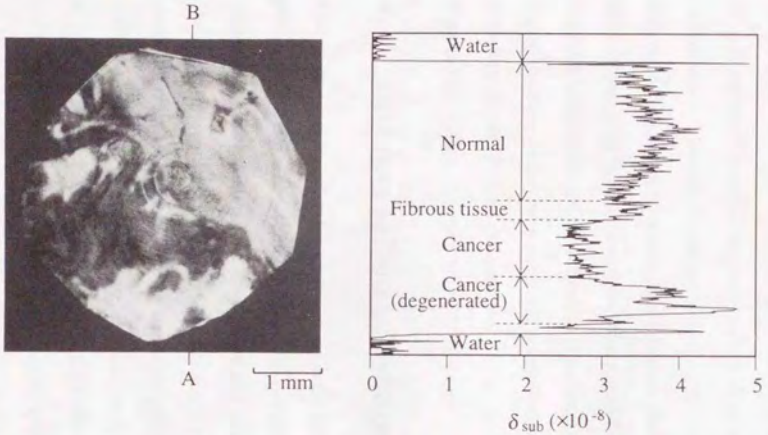

Fig. 4-10 (a) Another phase-contrast tomogram of the cancerous rabbit liver. (b) Contrast profile on the line AB. The δ_{sub} indicates the difference between the δ-values of the sample and water.

of the tumor.

More details of the observation result of the rabbit liver are discussed with Fig. 4-10; (a) is another tomogram, and (b) is the contrast profile on the line AB. Because the sample was observed in water, δ_{sub} indicates the difference in the δ-value between the sample and water. The true δ-value can be calculated by adding the δ-value of water for 0.7 Å X-rays, 7.4×10^{-7}, to δ_{sub}. The noise component (standard deviation of δ_{sub}) of the tomogram is at most 1.7×10^{-9}, estimating in the area where the inherent fine structure in the sample is not discernible. This means, therefore, that the difference of 5×10^{-9} (three times of the estimated standard deviation) is significantly differentiated with the present signal-to-noise ratio. As a result, it is concluded that 0.7% of the determination accuracy of the δ-value is achieved. This result will be used in the following discussions.

4.4 Interpretation of Image Contrast

The above result indicates that the present technique has the potential to depict cancer lesions and their pathological condition three-dimensionally without staining. As a next step, one must know the quantity which produces the image contrast, for quantitative analysis of phase-contrast tomograms. As mentioned, phase-contrast tomograms display the distribution of δ inside objects. In this section, the meaning of the contrast of phase-contrast X-ray CT is discussed more in detail. Based on the discussion, contrast effect of human blood is considered as another main contrast origin in biological systems.

In the hard X-ray region, the f_k^r in eq. (3.14) is much smaller than the atomic number Z_k, and therefore δ is approximately proportional to $\sum N_k Z_k$. Especially for light elements, the atomic mass is almost proportional to the number of electrons, and consequently $\sum N_k Z_k$ is approximately proportional to the specific

gravity. This means that the phase-contrast tomogram reveals the density distribution inside the object. Therefore, one can know from the observation result pictured in Figs. 4-9 and 4-10 that the density of the cancerous tissue is smaller than that of the normal liver tissue and, furthermore, increases depending on the degree of degeneration.

The observation result of the rat cerebellar slice described in Section 2.4 is consistent with above consideration. The specific gravity of lipid is smaller than those of the other parts of body. Therefore, the white matter looked dark in the phase-mapping image because it contains high density of myeline whose percentage of lipid is characteristically high (60%−70%) [22]. The artificial replacement of lipid with water actually decreased the contrast between the white matter and the granular layer.

The detection limit of the density deviation is estimated to be about 7 mg/cm^3 from the determination accuracy of δ described in Section 4.3. The amount of the detection limit makes us expect that blood distribution might be observable because red blood cells contain iron and the density is relatively high. Although this conjecture cannot be proved to be correct with *in vivo* observation at present, the effect of blood on phase-contrast images was evaluated by measuring δ-values of human blood and serum.

The liquid samples were put in a cell placed in one of the beam paths of the interferometer. The cell was made of acrylic resin whose wall at the side where the X-rays exit was inclined away from the entrance side (Fig. 4-11). The cell had two sections for testing with a reference sample.

Interference fringes like those in Fig. 4-12 were observed. The interference fringes at the center part of Fig. 4-12 were caused by the acrylic partition between the two sections, and the fringes on the both sides were caused by the liquids in the cell. The larger the δ of the sample is, the finer the interference fringes are. When the angle between the walls of the cell is α_w (see Fig. 4-11), the δ of the

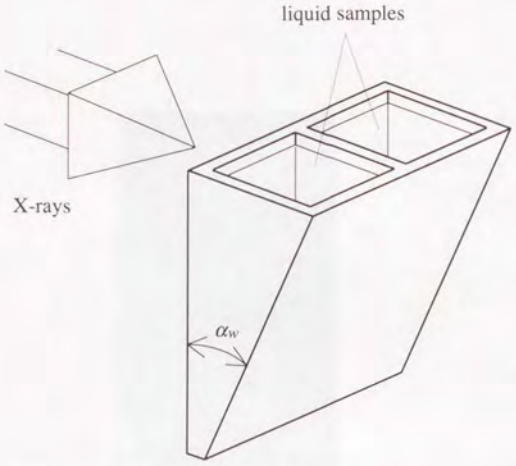

Fig. 4-11 The structure of the sample cell made of acrylic resin for the measurement of the refractive index of blood. The wall was 1 mm thick, and the X-ray exit side was at an incline.

sample in the cell is

$$\delta = \frac{\lambda}{l \tan \alpha_w}, \tag{4.1}$$

where l is the observed interval of the interference fringes. The value of α_w of the cell was 28 ± 0.4 degrees. Thus, the absolute value of δ was determined by measuring l.

We measured the δ's of distilled water, physiological salt solution and human blood with 0.7-Å, 0.8-Å and 0.92-Å X-rays. In addition, human blood was separated into serum and corpuscles and was also tested with 0.8-Å and 0.92-Å X-rays. We added 3.3% of heparin to the human blood sample to prevent

Fig. 4-12 An example of an interference pattern obtained with the cell shown in Fig. 4-11. The refractive index of the liquid sample in the cell was determined by measuring the interval of the fringes. The center part of the image was due to the acrylic partition. Both sides fringes were caused by the samples.

Table I Measured values of δ ($\times 10^{-6}$) with 0.7-Å, 0.8-Å and 0.92-Å X-rays.

λ (Å)	distilled water	physiological salt solution	serum	corpuscles	blood	acrylic resin
0.7	0.747	0.751	-	-	0.775	0.861
0.8	-	0.979	0.999	1.049	1.036	1.129
0.92	-	1.306	1.321	1.385	1.353	1.486

coagulation during measurement.

The measured values of δ from interference patterns are listed in Table I. The accuracy of the δ's depended on the accuracy of λ, α_w, and l, and was estimated to be within $\pm 2\%$. As to the relative value of δ between samples, the accuracy depended only on l because the influence by λ and α_w was canceled. Reading error of the fringe spacing l depended on how many fringes were observed, and was estimated to be within $\pm 0.5\%$. Therefore, the difference of δ among the samples was accurate within $\pm 0.5\%$.

In Fig. 4-13, δ/λ^2 is plotted against λ using the measured values in Table I. This is consistent in that δ is proportional to λ^2 (see eq.(3.14)). The difference of δ among the samples was significant. The δ of corpuscles was especially large; we expect this because corpuscles contain a high concentration of iron. To the contrary, the δ of serum was comparatively small. Consistent with this, the δ of blood was approximately 3% larger than that of serum because of the corpuscular ingredient in blood. The values of blood were more scattered than those of the other samples. It is likely that the corpuscular ingredient began to settle during measurement.

This result suggests that blood distribution in a body should produce a structure in a phase-contrast X-ray image. Although blood flows in all organs, the distribution of blood is different depending on the organ and the pathological

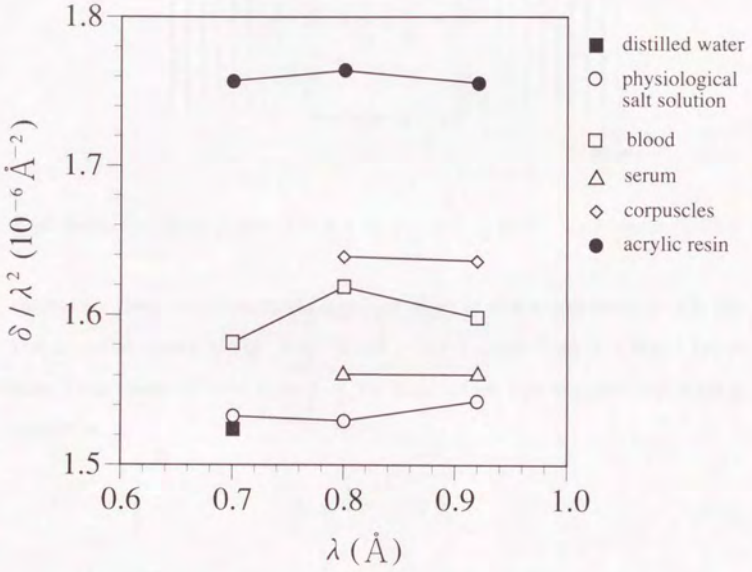

Fig. 4-13 Plot of δ/λ^2 versus λ using the measured values of δ in Table I.

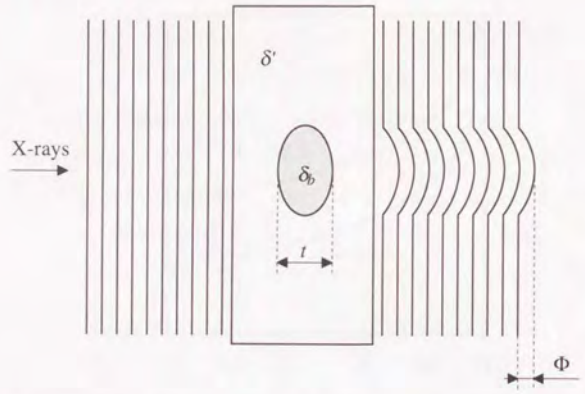

Fig. 4-14 The X-ray phase shift Φ is determined by δ_b, δ', and t (see eq. (4.2)).

condition. Here, we estimate the contrast effect of blood distribution with the simple model shown in Fig. 4-14. When a blood region such as a blood vessel exists in an organ whose δ value is δ', the X-ray phase shift Φ caused by blood is written as

$$\Phi = \frac{2\pi}{\lambda}(\delta_b - \delta')t, \tag{4.2}$$

where δ_b is the δ value of blood and t is the size of the blood region. Because organs contain blood throughout in their capillary vessels, we define

$$\delta' = c\delta_b + (1 - c)\delta_s, \tag{4.3}$$

where δ_s is the value of serum and c is the average density of blood in a organ (if $c = 1$, then $\delta' = \delta_b$ and if $c = 0$, $\delta' = \delta_s$). Thus, the δ of a tissue in the absence of blood is assumed to be the same as δ_s because the dominant origin of blood

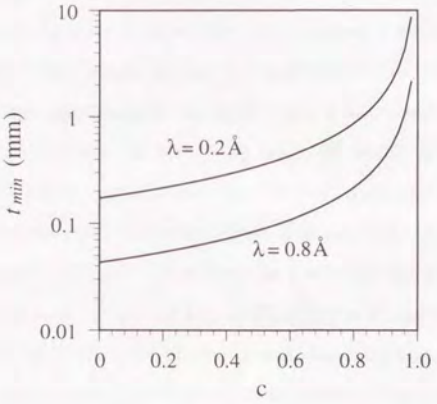

Fig. 4-15 The minimum thickness t_{min} observable by blood phase contrast. The c is the average blood density of the surrounding region. The curve for 0.8-Å X-rays was calculated from the measured data in Table I. The curve for 0.2-Å X-rays was estimated by using the relation, $\Phi \propto \lambda$.

contrast is red blood cells. From eqs.(4.2) and (4.3), the phase shift Φ is

$$\Phi = \frac{2\pi}{\lambda}(1-c)(\delta_b - \delta_s)t. \tag{4.4}$$

At the present signal-to-noise ratio of the phase-mapping images, the detection limit of the phase shift is estimated to be $2\pi/50$.* Therefore, the detectable minimum size t_{min} is

$$t_{min} = \frac{\lambda}{50(1-c)(\delta_b - \delta_s)}. \tag{4.5}$$

Figure 4-15 shows t_{min} calculated using the measured values for 0.8-Å X-rays.

*This value depends on the X-ray exposure used to obtain images.

For medical diagnostic use, an estimation for X-rays of shorter wavelength is necessary because the absorption of 0.8-Å X-rays is too large for investigation of the human body. Therefore, using the relation $\Phi \propto \lambda$, the curve for 0.2 Å , which is a typical average wavelength for diagnostic use, is also shown.

The value of c is not clear in a living body. However, a rough estimation from a capillary density may be possible. For example, the capillary volume ratio to the total volume in subendocadium of human left ventricle is reported to be approximately 50% [29]. Therefore, the c value in this case also might be approximately 50%. According to Fig. 4-15, a region a hundred microns thick might be detectable using blood phase contrast, assuming the present signal-to-noise ratio. As for the lateral direction, one can resolve 0.1-mm structures by the X-ray image sensor. Therefore, submillimeter spatial resolution by blood phase contrast in three-dimensional space might be achieved.

Thus, blood can affect the X-ray phase contrast. There are other materials that produce the X-ray phase contrast because the density is not uniform in the living systems. For diagnostic application, it is necessary to measure δ-values of other parts of body and to prepare a data table similar to the CT value table used for current diagnosis.

4.5 Future of Phase-Contrast X-Ray Imaging

It has been shown that phase-contrast X-ray CT is useful for observing biological soft tissues. For medical applications, however, some problems remain. The most crucial is widening of the observation area. The present observation area is limited by the size of the monolithic X-ray interferometer. One answer is to develop a separate-type X-ray interferometer to expand the spacing between the X-ray half-mirrors. Some papers [30–32] have described such X-ray interferometers that consist of two crystal blocks and an optical interferometer for their

alignment. Such X-ray interferometers were fabricated to measure precisely the silicon lattice constant, being independent of the X-ray wavelength. The third slab was separated, and the oscillation in the outgoing beam intensity was measured, transversing the independent third slab in the direction parallel to the diffraction vector. The displacement of the slab was measured by a laser interferometer with an accuracy of a subangstrom order. The techniques used in those X-ray/optical interferometers might be applied to phase-contrast X-ray CT with wider observation areas.

The scan time is another factor affecting the performance of the method. This depends on the X-ray beam intensity and on the spatial resolution that is required. We acquired images in Fig. 4-9 with 12-μm^3 voxels, taking about eight hours for the measurement. One way to shorten the scan time is to compromise the voxel size. For example, if the tomogram is reconstructed with 50-μm^3 voxels, the X-ray exposure will be reduced by 4^3 times because we are handling three-dimensional data. The time for the measurement is shorten also by using brighter X-ray source. The third-generation synchrotron facilities such as SPring-8, which is now under construction in Japan, will provide X-ray sources which meet this demand. However, for medical applications, it is also required that X-ray sources are compact. Unfortunately, such sources are not available to us at present, but it should be reminded that the phase-contrast technique is useful even for two-dimensional X-ray imaging (radiography). Because only one projection image is needed, the time required for the measurement is much smaller than that of phase-contrast X-ray CT. In this case, other types of X-ray sources than the SR sources might be available, and phase-contrast radiography for medical use might be practical. Then, radiographic diagnoses such as mammography and angiography might progress by being combined with the phase-contrast technique.

Phase-contrast imaging, furthermore, might offer advantages in observing stained objects. As mentioned, phase-contrast X-ray CT reveals the structure

inside nonstained objects. However, staining is a powerful approach because the contrast of an area of particular interest can be enhanced. In such observation, the high sensitivity of phase-contrast X-ray imaging would allow us to choose from a wide variety of contrast media; i.e., we would not be restricted to heavy materials for enhancement of the image contrast.

In this study, we concentrated on the observation of biological soft tissues. It is also evident that the phase-contrast technique may contribute to materials science. For example, the present technique is useful in evaluating the quality of composite organic materials, such as fiber reinforced plastics. For this purpose, however, higher spatial resolution is needed. The present resolution is worse than that of the X-ray image sensor. The author conjectures that the beam deflection described in Section 3.4 degraded the resolution. Although the tomograms were reconstructed on the planes where the effect of the deflection was smallest, the effect of the deflection especially in the direction perpendicular to the planes was not negligible. To improve the spatial resolution, it is necessary to develop a new technique, such as holographic tomography [33], taking into account the effect of the beam deflection caused by the sample.

Chapter 5

Concluding Remarks

This thesis described a novel idea for tomographic image reconstruction using X-ray phase information (phase-contrast X-ray computed tomography). The cross section of the X-ray phase shift is about a thousand times greater than that of X-ray absorption. Therefore, materials that do not absorb X-rays well, such as biological soft tissues, can be observed three-dimensionally without staining and without serious exposure to radiation. Biological soft tissues were observed with this novel technique using synchrotron X-rays. The results and conclusions of this study are mentioned as follows.

(1) Three-step phase-contrast X-ray imaging using an X-ray interferometer was described. The first step was the conventional technique of recording X-ray interference patterns on X-ray films. Phase-contrast X-ray images meant such interference patterns before the present study. Although the high sensitivity of phase-contrast X-ray imaging was clear, there was no evidence that the sensitivity was sufficient for the observation of biological soft tissues. As a preliminary study, we showed that the layer structure of a rat cerebellum was depicted in the interference pattern.

However, within this technique, the merit of high sensitivity was not fully utilized because quantitative understanding of the image was difficult. As the second step, techniques for obtaining an image of the phase shift dis-

tribution, or the phase-mapping image, were presented. Because the phase shift was the projection of the refractive index decrement δ, the structure appearing in the image was understood quantitatively.

As the third step, we developed phase-contrast X-ray CT which revealed the three-dimensional distribution of the refractive index inside an object using the phase-mapping images obtained in different projection directions by rotating the object.

(2) A cancerous tissue was observed with phase-contrast X-ray CT. The cancer lesion in the rabbit liver was clearly differentiated from the normal liver tissue, and the degree of degeneration in the tumor was also depicted. Moreover, fibrous tissues were observed in the marginal region of the tumor.

The value that creates the contrast in the phase-contrast tomograms was approximately proportional to the distribution of the density. The image contrast of the cancerous lesion, therefore, indicated that the density was smaller than that of normal tissue. Moreover, the tomogram showed that the density in the tumor increased depending on the degree of degeneration.

Phase-contrast X-ray CT might be available to investigate other tissues whose density is characteristically different. Estimating from the signal-to-noise ratio of the obtained image, the detection limit of the density deviation was 7 mg/cm^3.

(3) One attractive application target of phase-contrast X-ray CT is medical diagnostic use. Some problems of the present phase-contrast X-ray imaging with respect to medical diagnostic use were discussed. The observation area size is crucial at present. To investigate a body or a part of a body, an X-ray interferometer that produces a wide observation area must be developed. If a large silicon ingot is available, a system similar to the presented apparatus

may be constructed. However, the development of a larger ingot of a perfect silicon crystal may take much time. As an alternative, the author briefly mentioned separate type X-ray interferometers whose optical components are not monolithic. Basing on the technique used in such interferometers, the development of phase-contrast X-ray imaging of wide observation areas might be possible.

It is also necessary to shorten the scan time. The use of a brighter X-ray source is an ideal solution. Compromising the voxel size is another solution; the exposure is inversely proportional to the third power of the voxel size. Applications to two-dimensional cases such as mammography and angiography would be practical because these methods require an image from one projection direction. We are planning to develop the phase-contrast technique into medical applications of the two-dimensional cases first.

Acknowledgments

The work reported here was carried out at the Photon Factory of Japan's National Laboratory for High Energy Physics, under the proposal numbers 93-Y003, 93-Y008, 94-G144, and 95-Y005. The author would like to thank Professor Jun Fukuda of National Defense Medical School for the sample preparation and discussions in the beginning of this work. He is also grateful to Dr. Hideo Kawaguchi for the arrangement of the collaboration with Professor J. Fukuda. The author also wish to thank Dr. Tohoru Takeda and Professor Yuji Itai of the University of Tsukuba for the sample preparations and discussions. Thanks are also due to Drs. Yasushi Matsuzaki and Shinji Yoshiga of the University of Tsukuba for the preparation of the cancer lesions. He is deeply indebted to Dr. Keiichi Hirano at the Photon Factory for the experiments at the experimental station BL-14B.

The author would like to give thanks to Drs. Shojiro Asai (Director of Advanced Research Laboratory, Hitachi, Ltd.), Katsuki Miyauchi, Atsushi Suzuki, Akira Fukuhara, and Yasuharu Hirai for giving him the opportunity to conduct this research. He is also grateful to Drs. Tatsumi Hirano and Keiji Umetani for lending him the image sensor and so on.

Finally the author would like to express his sincere appreciation to Professor Seishi Kikuta of the University of Tokyo for the guidance and suggestions during the course of this thesis.

References

[1] G. N. Hounsfield, "Computerized transverse axial scanning (tomography). I. Description of system," *Brit. J. Radiol.*, **46**, 1016-1022 (1973).

[2] B. P. Flannery, H. W. Deckman, W. G. Roberge, and K. L. D'Amico, "Three-dimensional X-ray microtomography," *Science*, **237**, 1439-1444 (1987).

[3] U. Bonse, R. Nusshardt, F. Busch, R. Pahl, J. H. Kinny, Q. C. Johnson, R. A. Saroyan, and M. C. Nichols, "X-ray tomographic microscopy of fibre-reinforced materials," *J. Mater. Sci.*, **26**, 4076-4085 (1991).

[4] J. H. Kinny and M. C. Nichols, "X-ray tomographic microscopy (XTM) using synchrotron radiation," *Annu. Rev. Sci.*, **22**, 121-152 (1992).

[5] J. H. Kinny, T. M. Breunig, T. L. Starr, D. Haupt, M. C. Nichols, S. R. Stock, M. D. Butts, and R. A. Saroyan, "X-ray tomographic study of chemical vapor infiltration processing of ceramic composites," *Science*, **260**, 789-792 (1993).

[6] P. Spanne, J. F. Thovert, C. J. Jacquin, W. B. Lindquist, K. W. Jones, and P. M. Adler, "Synchrotron computed microtomography of porous media: topology and transports," *Phys. Rev. Lett.*, **73**, 2001-2004 (1994).

[7] T. Hirano, K. Usami, Y. Tanaka, and C. Masuda, "*In situ* x-ray CT under tensile loading using synchrotron radiation," *J. Mater. Res.*, **10**, 381-386 (1995).

[8] *Handbook on synchrotron radiation*, edited by S. Ebashi, M. Koch, and E. Rubenstein (Elsevier, The Netherlands, 1991).

[9] U. Bonse and M. Hart, "An X-ray interferometer with long interfering beam paths," *Appl. Phys. Lett.*, **7**, 99-101 (1965).

[10] M. Ando and S. Hosoya, "An attempt at X-ray phase-contrast microscopy," *Proc. 6th International Conference of X-ray Optics and Microanalysis*, edited by G. Shinoda, K. Kohra, and T. Ichinokawa (University of Tokyo 1972), pp. 63-68.

[11] P. Spieker, M. Ando, and S. Suzuki, "Phase and absorption contrast investigation of a human tooth," *Annu. Meet. Jpn. Soc. Phys.*, 404 (1983).

[12] U. Bonse, and M. Hart, "An X-ray interferometer," *Appl. Phys. Lett.*, **6**, 155-156 (1965).

[13] R. A. Brooks and G. D. Chiro, "Principles of computer assisted tomography (CAT) in radiographic and radioisotopic imaging," *Phys. Med. Biol.*, **21**, 689-732 (1976).

[14] J. Radon, "On the determination of functions from their integrals along certain manifolds," *Ber. Verh. Sächs Akad. Wiss.*, **69**, 262-277 (1917).

[15] A. C. Thompson and J. Llacer, "Computed tomography using synchrotron radiation," *Nucl. Instrum. Methods*, **222**, 319-323 (1984).

[16] B. W. Batterman and H. Cole, "Dynamical diffraction of X-rays by perfect crystals," *Mod. Phys.*, **36**, 681-717 (1964).

[17] O. Larsell and J. Jansen, *The comparative anatomy and histology of the cerebellum* (University of Minnesota, Minneapolis, 1972).

[18] S. W. Ranson and S. L. Clark, *The anatomy of nervous system* (Saunders, Philadelphia, 1959), p. 274.

[19] M. Takeda, H. Ina, and S. Kobayashi, "Fourier-transform method of fringe-pattern analysis for computer-based topography and interferometry," *J. Opt. Soc. Am.*, **72**, 156-160 (1982).

[20] J. H. Bruning, D. R. Herriott, J. E. Gallagher, D. P. Rosenfeld, A. D. White, and D. J. Brangaccio, "Digital wavefront measuring interferometer for testing optical surfaces and lenses," *Appl. Opt.*, **13**, 2693-2703 (1974).

[21] Y. Suzuki, K. Hayakawa, K. Usami, T. Hirano, T. Endoh, and Y. Okamura, "X-ray sensing pickup tube," *Rev. Sci. Instrum.*, **60**, 2299-2302 (1989).

[22] E. Eichberg, G. Hauser, and M. L. Karmovsky, *The structure and function of nervous tissue*, edited by G. H. Bourne (Academic, New York, 1969), p. 185.

[23] G. N. Ramachandran and A. V. Lakshminarayanan, "Three-dimensional reconstruction from radiographs and electron micrographs: application of convolutions instead of Fourier transforms", *Proc. Nat. Acad. Sci. USA*, **68**, 2236-2240 (1971).

[24] R. W. James, *The optical principles of the diffraction of X-rays* (G. Bell and Sons, London, 1950).

[25] S, Sasaki, *Numerical tables of anomalous scattering factors calculated by the Cromer and Liberman's method*, KEK Report 88-14, National Laboratory for High Energy Physics (1989).

[26] S. Sasaki, *X-Ray absorption coefficients of the elements (Li to Bi, U)*, KEK Report 90-16, National Laboratory for High Energy Physics (1990).

[27] J. H. Bruning, *Optical shop testing* (Wiley-Interscience, New York, 1978), p. 414.

[28] G. Borrmann, G. Hildebrant, and H. Wagner, "Röntgenstrahl-Fächer im Kalkspar," *Z. Phys.*, **142**, 406-414 (1955).

[29] O. Hudlicka, *Development of microcirculation: capillary growth and adaptation* Handbook of physiology, Sect. II., Cardiovascular system Vol. 4, microcirculation system part I, edited by E. M. Renkin and C. C. Michel (American physiological society, Bethesda, Maryland, 1984), pp. 165-172.

[30] R. D. Deslattes and A. Henins, "X-ray to visible wavelength ratios," *Phys. Rev. Lett.*, **31**, 972-975 (1973).

[31] P. Becker, K. Dorenwendt, G. Ebeling, R. Lauer, W. Lucas, R. Probst, H. Rademacher, G. Reim, P. Seyfried, and H. Siegert, "Absolute Measurement of the (220) Lattice plane spacing in a silicon crystal," *Phys. Rev. Lett.*, **46**, 1540-1543 (1981).

[32] M. Tanaka and K. Nakayama, "A new optical interferometer for absolute measurement of linear displacement in the subnanometer range," *Jpn. J. Appl. Phys.*, **22**, L233-L235 (1983).

[33] I. McNulty, "The future of X-ray holography," *Nucl. Instrum. Meth.*, A**347**, 170-176 (1994).

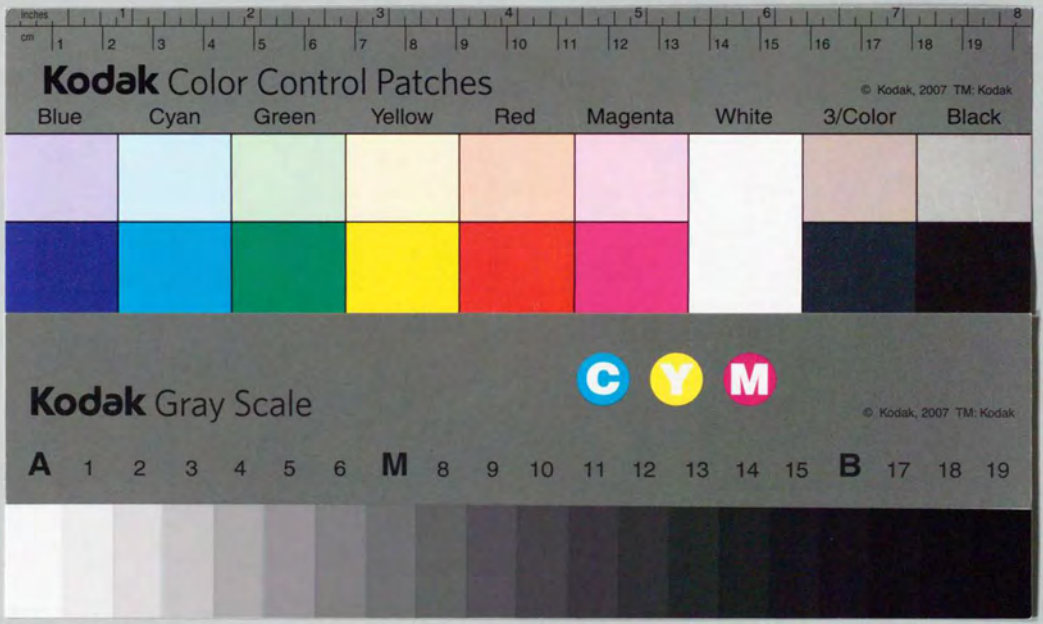
inches
cm
Kodak Color Control Patches
© Kodak, 2007 TM: Kodak
Blue
Cyan
Green
Yellow
Red
Magenta
White
3/Color
Black
Kodak Gray Scale
C
Y
M
© Kodak, 2007 TM: Kodak
A 1 2 3 4 5 6 M 8 9 10 11 12 13 14 15 B 17 18 19